

# UC Riverside

## UC Riverside Electronic Theses and Dissertations

### Title

Enzyme Mediated Synthesis of a Semiconducting Metal Oxide

### Permalink

<https://escholarship.org/uc/item/4tf7w1pg>

### Author

Johnson, John Michael

### Publication Date

2012

Peer reviewed|Thesis/dissertation

UNIVERSITY OF CALIFORNIA  
RIVERSIDE

Enzyme Mediated Synthesis of a Semiconducting Metal Oxide

A Thesis submitted in partial satisfaction  
of the requirements for the degree of

Master of Science

in

Chemical and Environmental Engineering

by

John Michael Johnson

September 2012

Thesis Committee:

Dr. David Kisailus, Chairperson

Dr. Charles Wyman

Dr. Jiayu Liao

Copyright by  
John Michael Johnson  
2012

The Thesis of John Michael Johnson is approved:

---

---

---

Committee Chairperson

University of California, Riverside

## ABSTRACT OF THE THESIS

Enzyme Mediated Synthesis of a Semiconducting Metal Oxide

by

John Michael Johnson

Master of Science, Graduate Program in Chemical and Environmental Engineering  
University of California, Riverside, September 2012  
Dr. David Kisailus, Chairperson

Enzymes are an important class of biological molecules, their specific functionality being exploited to perform tasks beyond the reach of conventional chemistry. Because they are operational under environmentally friendly, ambient conditions, the adaptation of these biomacromolecules can be used to replace current energy intensive and environmentally harsh synthesis methods for materials applications. One possible use of the enzyme urease is to modify the solution environment of a water soluble and stable  $\text{TiO}_2$  precursor under benign conditions. The intended result of this process would be to yield  $\text{TiO}_2$  nanostructures of controlled size. These  $\text{TiO}_2$  nanostructures can be utilized for numerous engineering applications such as low cost photovoltaics and photocatalysis. The motivation behind this work is to produce titanium dioxide using an ambient temperature, near neutral pH, one-pot synthesis method. Furthermore to make this process suitable for industrial application this work also focuses on immobilizing the enzyme for increased stability and reusability.

## TABLE OF CONTENTS

<b>Chapter 1. Introduction and Background.....</b>	<b>1</b>
1.1 Introduction.....	1
1.2 The role of nanocrystalline TiO <sub>2</sub> in energy production.....	1
1.3 Photocatalytic degradation of organic contaminants using nanocrystalline TiO <sub>2</sub> .....	5
<b>Chapter 2. Principles and Preparation of Titanium Dioxide Nanocrystals.....</b>	<b>8</b>
2.1 Properties of Titanium Dioxide.....	8
2.2 Vapor phase methods of TiO <sub>2</sub> synthesis.....	10
2.2.1 Chemical vapor deposition.....	10
2.2.2 Physical vapor deposition.....	10
2.2.3 Flame pyrolysis.....	11
2.3 Solution-based Synthesis of Nanocrystalline TiO <sub>2</sub> .....	11
2.3.1 Decomposition of organo-metallic compounds: sol-gel synthesis.....	13
2.3.2 Forced hydrolysis: hydrothermal/solvothermal synthesis.....	14
2.3.3 Controlled release of hydroxide ions: urea hydrolysis.....	15
2.4 Concluding Remarks.....	16
<b>Chapter 3. Urease Mediated Synthesis of Titanium Dioxide Nanocrystals.....</b>	<b>17</b>
3.1 Lessons from Nature.....	17
3.2 Experimental/Discussion.....	21
3.2.1 General Methods.....	21
3.2.2 Urease activity: Michaelis-Menten analysis at varying temperatures.....	23
3.2.3 Urease mediated synthesis of TiO <sub>2</sub> .....	26
3.2.4 Urease mediated synthesis of TiO <sub>2</sub> : temperature study.....	29
3.2.5 Urease mediated synthesis of TiO <sub>2</sub> : time study.....	40
3.2.6 Urease mediated synthesis of TiO <sub>2</sub> : precursor concentration study.....	48

3.2.7 Room temperature $\text{TiO}_2$ synthesis using exogenous pH adjustment.....	53
3.3 Discussion/Conclusion.....	55
<b>Chapter 4. Immobilized Urease Mediated Synthesis of <math>\text{TiO}_2</math>.....</b>	<b>61</b>
4.1 Enzyme Immobilization.....	61
4.2 Experimental/Discussion.....	64
4.2.1 Verification of urease immobilization.....	65
4.2.2 Reusability of urease conjugated gold substrate.....	68
4.2.3 Synthesis of $\text{TiO}_2$ using immobilized urease.....	70
4.3 Discussion/Conclusion.....	72
<b>Chapter 5. Summary.....</b>	<b>74</b>

## LIST OF FIGURES

Figure 1.1	2011 BP Statistical Review of World Energy.....	2
Figure 1.2	Photoexcitation of a semiconductor.....	3
Figure 1.3	Dye-sensitized solar cell.....	4
Figure 1.4	Semiconductor photocatalysis.....	5
Figure 2.1	Titanium dioxide octahedron.....	8
Figure 2.2	Anatase and rutile octahedral arrangements.....	8
Figure 2.3	Hydrated $Ti^{4+}$ cation.....	11
Figure 2.4	Oxolation of saturated $Ti^{4+}$ cation.....	20
Figure 3.1	Structure of the urease enzyme.....	20
Figure 3.2	Hydrolysis of TiBALDH molecule.....	21
Figure 3.3	Change in ammonium ion concentration with respect to time.....	24
Figure 3.4	Michaelis-Menten and Lineweaver-Burke analysis.....	25
Figure 3.5	XRD and EDS analysis of urease mediated synthesized $TiO_2$ .....	27
Figure 3.6	XRD analysis of urease mediated $TiO_2$ synthesis: Temperature Study..	30
Figure 3.7	TEM analysis of urease mediated $TiO_2$ synthesis: 25°C.....	31
Figure 3.8	TEM analysis of urease mediated $TiO_2$ synthesis: 40°C.....	32
Figure 3.9	TEM analysis of urease mediated $TiO_2$ synthesis: 60°C.....	33
Figure 3.10	Diffuse reflectance analysis: temperature study.....	34
Figure 3.11	La Mer diagram.....	35
Figure 3.12	Change in Gibbs free energy with respect to crystallite radius.....	36

Figure 3.13	Effect of temperature on Gibbs free energy.....	37
Figure 3.14	XRD analysis: temperature study (60°C, 80°C, and 100°C).....	39
Figure 3.15	XRD analysis: time study (12hr, 24hr, and 36hr).....	41
Figure 3.16	TEM analysis: time study (12hr).....	42
Figure 3.17	TEM analysis: time study (24hr).....	43
Figure 3.18	TEM analysis: time study (36hr).....	44
Figure 3.19	pH with respect to time: time study.....	45
Figure 3.20	TEM analysis: time study (1hr).....	46
Figure 3.21	TEM analysis: time study (6hr).....	47
Figure 3.22	XRD analysis: 0.001M, 0.01M, and 0.1M TiBALDH concentration.....	49
Figure 3.23	TEM analysis: 0.001M TiBALDH.....	50
Figure 3.24	TEM analysis: 0.01M TiBALDH.....	51
Figure 3.25	TEM analysis: 0.1M TiBALDH.....	52
Figure 3.26	TEM analysis: exogenous pH adjustment.....	54
Figure 4.1	Schematic of immobilization procedure.....	63
Figure 4.2	pH with respect to time: immobilized urease.....	65
Figure 4.3	AFM of urease conjugated gold substrate.....	67
Figure 4.4	Schematic diagram of urease hexameric structure.....	68
Figure 4.5	Immobilized urease: Reusability study.....	70
Figure 4.6	TEM analysis: immobilized, urease mediated TiO <sub>2</sub> synthesis.....	71

## Chapter 1: Introduction and Background

### *1.1 Introduction*

Nanocrystalline titanium dioxide ( $\text{TiO}_2$ ) exhibits optoelectronic properties attractive for a wide range of applications such as hydrogen storage<sup>1</sup>, gas sensing<sup>2</sup>, heterogeneous photocatalysis<sup>3</sup>, and electrodes in Dye-sensitized solar cells (DSSCs)<sup>4</sup>.  $\text{TiO}_2$  is an ideal material for these applications due to its chemical and physical stability in aqueous media, natural abundance and minimal impact on the environment. Although  $\text{TiO}_2$  occurs naturally as three polymorphs (brookite, rutile, and anatase), nanoscale crystalline  $\text{TiO}_2$  often requires extensive processing at elevated temperatures and/or in many instances, the use of caustic or environmentally unfriendly solvents. Vapor phase synthesis methods of  $\text{TiO}_2$  such as chemical vapor deposition (CVD)<sup>5</sup>, physical vapor deposition (PVD)<sup>6</sup>, and flame pyrolysis<sup>7</sup> are energy-intensive and commonly result in the production of large, low-surface area crystals. Lower temperature solution-based routes such as hydrothermal<sup>8</sup>, solvothermal<sup>9</sup>, and sol-gel<sup>10</sup> methods have also been proven effective for the synthesis of metal-oxide nanostructures but generally offer little control over size distribution of resulting materials.

### *1.2 The role of nanocrystalline $\text{TiO}_2$ in energy production*

Based on current levels of consumption, proven reserves of petroleum, natural gas and coal are expected to deplete over the next 42, 60, and 122 years<sup>11</sup>, respectively. At the same time, an increasing population alongside the increasing industrialization of

developing nations is expected to result in a substantial rise, to nearly double the amount used in the year 2000 by the year 2030<sup>12</sup>, in worldwide energy consumption (fig. 1).

Reliance on fossil fuels can be reduced by the introduction of new and/or renewable sources of energy<sup>13</sup> (i.e., biofuels<sup>14</sup>, wind<sup>15</sup>, geothermal<sup>16</sup>, solar<sup>17</sup>, etc.). Solar energy is one such renewable

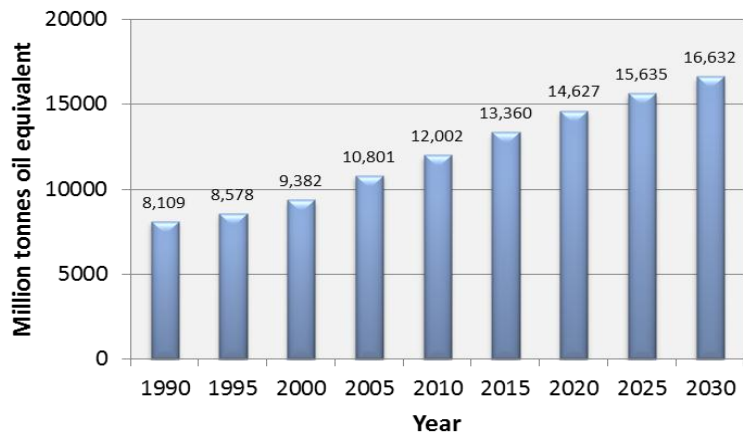
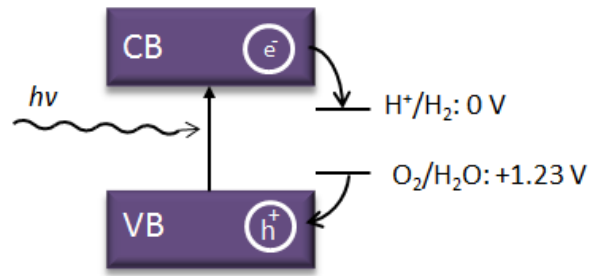


Figure 1.1: 2011 BP statistical review of world energy.

source that, when used in tandem with a semiconducting material can be converted directly into electrochemical energy, as well as used for the production of hydrogen fuel. Among these, solar energy is especially attractive due to abundance of energy available for capture. The sun delivers  $4 \times 10^{24}$  J of solar energy to the Earth annually<sup>18</sup> which is substantially higher than the  $1.5 \times 10^{21}$  J of energy consumed worldwide in 2009<sup>19</sup>. Although there is an abundance of solar energy available, current technologies are either too inefficient or too expensive to vie with fossil fuels. Therefore, new, low cost technologies, utilizing semiconducting nanomaterials such as  $\text{TiO}_2$ , are needed in order to compete with fossil fuels.

Photoexcitation of a semiconducting material proceeds due to radiation exposure when the energy of the radiation is greater than the energy of the band-gap<sup>20</sup>. The band gap represents the energy difference



**Figure 1.2: Schematic diagram of photoexcitation of electron from valence band (VB) to conduction band (CB) in a semiconducting material.**

between the valence band (VB) of electrons and the conduction band (CB). Excitation of an electron to the conduction band liberates the electron allowing free movement along the atomic lattice of the semiconductor<sup>21</sup>. Shown schematically in figure 1.2, the absorption of the photon will result in the production of an exciton (an electron/hole pair) and subsequent charge separation of the electron/hole pair as the electron is excited into the conduction band of the semiconductor<sup>22</sup>. This process can be utilized for application in water-splitting to produce hydrogen fuel<sup>23</sup>. Hydrogen fuel is a clean burning, renewable source of energy with a heat of combustion greater than 2.5 times that of hydrocarbon fuels<sup>24</sup>. For the case where the bottom level of the conduction band is more negative than the reduction potential of  $H^+/H_2$  and the top of the valence band is more positive than the oxidation potential of  $O_2/H_2O$  then water splitting proceeds by the reduction of water molecules by electrons to form  $H_2$  and the oxidation of water molecules by holes to form  $O_2$ <sup>25</sup>.

In order to convert solar energy directly into electrochemical energy, Michael Gratzel demonstrated a photovoltaic cell based on the dye-sensitization of colloidal TiO<sub>2</sub> films<sup>26</sup>. A schematic of a dye-sensitized solar cell (DSSC) based on Gratzel's pioneering research is shown in figure 1.3. A photo-responsive organic dye molecule is adsorbed onto the surface of a

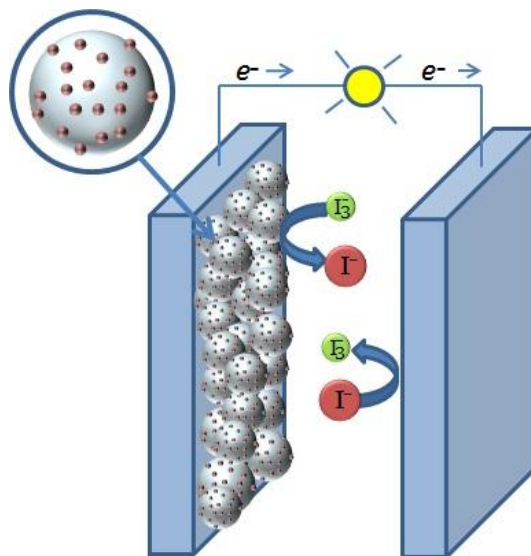


**Figure 1.3: Schematic diagram of a dye-sensitized solar cell (DSSC).**

semiconducting material such as TiO<sub>2</sub>. The dye-modification of the TiO<sub>2</sub> nanocrystalline surface enables electrons in the dye molecule, excited by photons, direct transport into the conduction band of the TiO<sub>2</sub>. The organic dye may be treated as a narrow band semiconductor with photoexcitation occurring between the highest occupied molecular orbital (HOMO) and the lowest unoccupied molecular orbital (LUMO)<sup>27</sup>. The photo-induced current can then drive a load by electron transmission through an attached circuit. An electrolyte, containing a redox pair such as I<sub>3</sub><sup>-</sup>/I<sup>-</sup>, enables the restoration of the dye molecules<sup>28</sup>. The schematic illustrates that at the counter electrode surface, the iodide ion is reduced to triiodide ion. The triiodide ion will then regenerate the dye molecules in order to continue the reaction cycle. The reaction scheme for excitation, electron injection and dye regeneration is thus<sup>29</sup>.





### 1.3 Photocatalytic degradation of organic contaminants in waste water using nanocrystalline TiO<sub>2</sub>

Increasing worldwide population, coupled with industrial development, is placing growing pressure on worldwide water resources through both increased consumption and by introduction of new, as yet, unregulated classes of organic pollutants known as emerging contaminants. Emerging contaminants

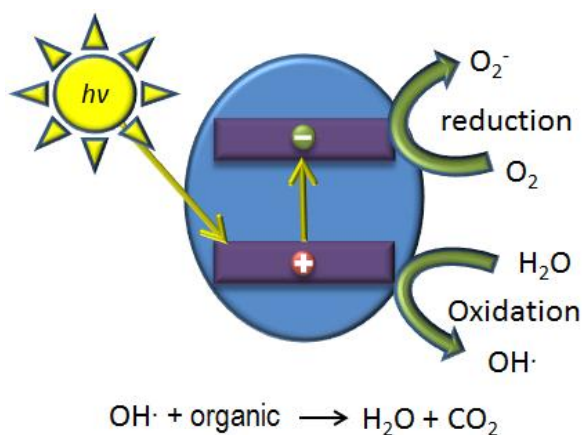


Figure 1.4: Schematic diagram of semiconductor photocatalysis.

refer to those compounds that, based on several criteria, may present a future risk to either humans, animals, or the environment but current data is ambiguous, either due to lack of available studies, or insufficient technology to properly quantify the environmental fate of the contaminants<sup>30</sup>. Two classes of emerging contaminants currently under scrutiny are pharmaceuticals and endocrine disrupting compounds (EDCs). Pharmaceuticals, both prescription and over the counter drugs, are excreted as metabolites of parent chemicals after use by both humans and animals<sup>31,32</sup>. EDCs are chemicals, synthetic or naturally occurring, that can alter the functioning of an organisms

natural hormonal control systems<sup>33</sup>. As conventional water treatment methods fail to completely remove these new classes of pollutants from waste treatment effluent streams, there is a corresponding increase in these chemicals being found in both ground and surface water<sup>34,35</sup>. Thus, new treatment methods, such as heterogeneous photocatalysis, are needed to ensure clean and safe drinking water<sup>36</sup>.

Heterogeneous photocatalysis is an advanced oxidation process (AOP), for use in water treatment, using the photoexcitation of a semiconductor (e.g., TiO<sub>2</sub>) to degrade organic contaminants<sup>37</sup>. As described previously the photo-excitation by radiation of higher energy than that of the band gap will result in the transmission of an electron to the conduction band of the semiconductor (fig. 1.4). The remaining hole in the valence band acts as an oxidizing agent reacting with either an adsorbed water molecule on the surface or with surface OH<sup>-</sup> groups to form an ·OH radical while the conduction band transmitted electron will reduce oxygen present in the system to a superoxide anion O<sub>2</sub><sup>·38</sup>. The ·OH radical acts as a strong oxidizing agent and will react with organic constituents. Intermediates formed in these reactions will be further oxidized by the ·OH radical resulting in the final products CO<sub>2</sub> and H<sub>2</sub>O<sup>39</sup>.

Nanocrystalline TiO<sub>2</sub> has also been studied for use in electrochromic windows and displays, hydrogen storage, and sensing applications. Electrochromic devices depend on the on the redox potential of a material inducing a color change in the material on excitation of the valence band electrons to the conduction band<sup>25</sup>. With respect to hydrogen storage it has been demonstrated that near 2wt % H<sub>2</sub> could be stored using TiO<sub>2</sub>

nanomaterials at room temperature 6MPa pressure<sup>40</sup>. Subsequently 75% of the stored hydrogen was released on lowering of the pressure to ambient conditions. TiO<sub>2</sub> nanomaterials have also been studied for use in gas-sensing applications. Nanocrystalline TiO<sub>2</sub> has been proven to be highly sensitive in application for sensing H<sub>2</sub><sup>41</sup> and NO<sub>2</sub><sup>42</sup>, and is also considered promising for application in sensing gaseous carbon monoxide<sup>43</sup>, methanol and ethanol<sup>44</sup>.

## Chapter 2: Principles and Preparations of Titanium Dioxide Nanocrystals

### 2.1 Properties of Titanium Dioxide

As shown in figure 2.1, each  $\text{Ti}^{4+}$  ion is surrounded by a six  $\text{O}^{2-}$  octahedron.  $\text{TiO}_2$  occurs naturally as the minerals rutile (fig. 2.2A), anatase (fig. 2.2B), and brookite<sup>45</sup>. Although both rutile and anatase  $\text{TiO}_2$  share the octahedral structure they differ in both the distortion and the orientation of octahedra in the superstructure<sup>46</sup>. The rutile structure of  $\text{TiO}_2$  is indicated by the presence of two edge shared and eight corner shared octahedra. Rutile is

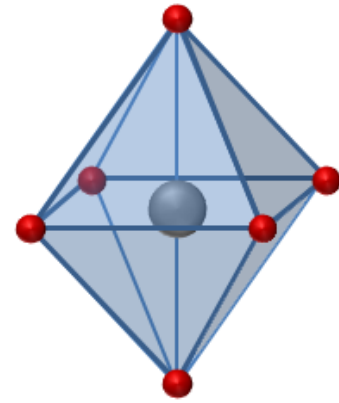


Figure 2.1: Schematic representation of a  $\text{TiO}_6$  octahedron, grey indicating titanium and red indicating coordinated oxygen atoms.

considered the most stable phase, occurring naturally under high temperature and pressure in igneous and metamorphic rock formations. Anatase and brookite are polymorphs of the more common rutile phase. Anatase consists of four edge-shared and four corner-shared octahedral, while the brookite structure consists of three edge-shared octahedra, forming an orthorhombic structure.  $\text{TiO}_2$  is a wide-band gap semi-conducting material with associated band gaps of 3.0eV

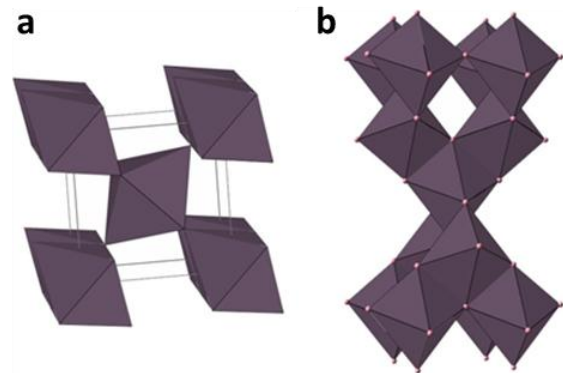


Figure 2.2: Illustrations of A) rutile and B) anatase  $\text{TiO}_6$  octahedral arrangements.

(corresponding to a wavelength,  $\lambda$  of 410nm) and 3.2eV ( $\lambda = 385\text{nm}$ ) for rutile and anatase, respectively<sup>47</sup>.

Other semi-conducting materials have been demonstrated as feasible constituents in photocatalytic application but with several important drawbacks. Non-oxide semiconductors such as GaAs<sup>48</sup>, CdS<sup>49</sup>, and CdSe<sup>50</sup> have been demonstrated as viable materials for solar energy conversion. However, these same materials show a tendency towards photoanodic decomposition, a phenomenon known as photocorrosion, and are considered environmentally toxic<sup>51</sup>. ZnS is another transition metal sulfide that has been considered as a possible alternative to TiO<sub>2</sub> due to its optical response in visible light when doped with transition or rare earth metal ions<sup>52</sup>. Mass application of ZnS photocatalysts are still limited by the high cost of production as well as difficulties in the separation and recycling of the constituent ores<sup>53</sup>. Another metal oxide that has been studied extensively for photocatalytic application is ZnO. ZnO is a wide band gap semiconductor (3.37eV) but has been shown to be unstable in aqueous solution decomposing to form Zn(OH)<sub>2</sub> on the ZnO surface thus reducing activity of the photocatalyst over time<sup>54</sup>. Compared to these other materials, TiO<sub>2</sub> has been shown to be photocatalytically stable with respect to photocorrosion and chemical corrosion, and is abundantly available in nature (thus the raw materials are inexpensive). Thus, TiO<sub>2</sub> is considered to be environmentally friendly<sup>55</sup> and continues to be the subject of intense study for use in photoelectrochemical and photocatalytic applications.

## *2.2 Vapor phase methods of TiO<sub>2</sub> Synthesis*

### *2.2.1 Chemical Vapor Deposition*

Chemical vapor deposition (CVD) refers to a method of condensing vapor phase reagents that react on a substrate to form a thin film or nanostructured materials. A typical CVD process involves the influx of a precursor gas into a vacuum chamber at temperatures ranging from 200-1600°C<sup>56</sup>. The chemical precursors most commonly used in CVD production of TiO<sub>2</sub> are titanium tetrachloride (TiCl<sub>4</sub>) and titanium tetrakisopropoxide (TTIP)<sup>57</sup>. For instance, Kim and coworkers demonstrated the synthesis of 3 – 29nm TiO<sub>2</sub> nanoparticles by the thermal decomposition of TTIP and the oxidation of TiCl<sub>4</sub> using a CVD process with temperatures in the range of 1200°C<sup>58</sup>. The sizes of TiO<sub>2</sub> nanoparticles were controlled by both the total flow rate of the precursors and the precursor concentrations.

### *2.2.2 Physical Vapor Deposition*

Physical Vapor Deposition (PVD) proceeds similarly to CVD with the exception that no chemical reaction occurs. Typically, a vacuum chamber operating at a temperature of 850°C and a pressure of near 300Torr are used to synthesis TiO<sub>2</sub> nanostructures from pure Titanium metal powders<sup>59</sup>.

### 2.2.3 Flame Pyrolysis

In the flame pyrolysis method an aerosolized titanium precursor is combusted. The flame temperature (generally  $\sim 850^{\circ}\text{C}$ ) is maintained by controlling the influx of oxygen and natural gas into the system<sup>60</sup>. In this vapor combustion process, the ligands are oxidized and the resulting Ti-O moieties condense to form metal-oxide nuclei. Further growth continues by consumption of embryonic metal-oxide clusters within the vapor phase<sup>61</sup>. Flame pyrolysis is used to synthesize Degussa P25, considered the standard, commercially-based  $\text{TiO}_2$  used for photocatalytic studies<sup>62</sup>. It has been found that regulation of both the flame temperature as well as precursor concentration offer control over the final phase and particle size of the  $\text{TiO}_2$  nanomaterials.

### 2.3 Solution-based synthesis of nanocrystalline $\text{TiO}_2$

The size and composition of the nano-crystalline  $\text{TiO}_2$  is of primary importance to photocatalytic applications since the efficiency of producing radicals will depend on the availability of active sites<sup>39</sup>.

Intuitively, smaller particles will have a larger surface area to volume ratio and thus will present a larger catalytic surface area, increasing

the net charge carrier production rate. A negative consequence of the smaller nanocrystalline  $\text{TiO}_2$  is the recombination of electrons and holes due to multiple surface traps<sup>63</sup>. Efficiency for a given photocatalytic application is generally based on a trade-off between the charge carrier transfer rate and the rate of electron-hole recombination.

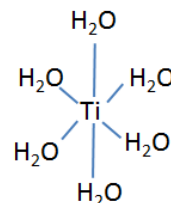


**Figure 2.3:** Schematic diagram of a fully hydrated  $\text{Ti}^{4+}$  cation.

Solution based methods allow control over the synthesis at a molecular level, allowing researchers to direct the morphology, size and homogeneity of the prepared materials<sup>64</sup>.

For a metal cation  $M^{Z+}$  dissolved in pure water, solvation will occur by the surrounding water molecules<sup>65</sup>. Figure 2.3 shows a fully hydrated  $Ti^{4+}$  cation. For the coordinatively saturated  $Ti^{4+}$  cation, the formation of crystalline  $TiO_2$  proceeds via a condensation reaction referred to as oxolation, named for the formation of an *oxo-bridge*

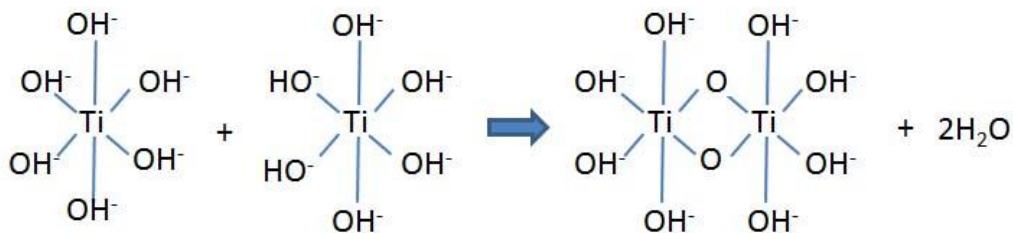


Figure 2.4: Schematic diagram of the oxolation of a fully saturated  $Ti^{4+}$  ion.

(-O-) between two metal centers, and given by the following reaction sequence for a generic metal center and by figure 2.4 for the saturated  $Ti^{4+}$  cation<sup>66</sup>. Equation 2.1 shows the nucleophilic addition of two saturated metal cations followed by the elimination of water to form the M-O-M bond (eqn. 2.2).



Solution based synthesis methods rely on the hydrolysis/condensation sequence to produce crystalline materials. There are three primary routes to hydrolyze a metal oxide for subsequent condensation: *decomposition of organo-metallic compounds*, *forced hydrolysis*, and *controlled release of hydroxide ions*.

### 2.3.1 Decomposition of Organo-metallic Compounds: Sol-gel Synthesis

Metal alkoxides readily react in water to form metal hydroxides or hydrated oxides according to the following reaction<sup>67</sup>:



As shown in reaction (2.3), the alkoxide groups (-OR) undergo nucleophilic attack by oxygen atoms present in water molecules. The alkoxide groups are thus replaced resulting in the formation of a metal hydroxide species. The hydrolysis of the metal or metal hydroxide (eqn. 2.3) is followed by polycondensation (eqns. 2.4 and 2.5) reactions to form colloidal particles.



Equation 2.4 is representative of an alkoxolation reaction (release of an alcohol). As discussed previously the release of a water molecule and formation of an -oxo- bridge between two metal cations is termed an oxolation reaction (eqns. 2.1 & 2.2). The result of these processes is the formation of a network of interlocked -O-M-O-M- chains. Over time this network becomes large enough and nucleates as particles in solvent (sol). The solvent is removed and aging of the gel allows polycondensation to continue, resulting in an overall reduction in the size of the gel and removal of remaining solution (syneresis), further, densifying the gel. In general the hydrolysis and condensation of metal oxide precursors used in sol-gel synthesis proceed very rapidly, thus reducing control over the

composition and homogeneity of the final product<sup>68</sup>. Adjustment of reaction parameters such as solution pH and temperature as well as the water:precursor ratio allows for manipulation of the solubility and surface chemistry of the colloidal particles thus introducing some control with respect to the end-point nano-structure<sup>69</sup>. Sol-gel synthesis largely produces amorphous precipitates and thus is followed by calcination at high temperatures, 400 - 800°C, to produce crystalline materials. Nevertheless, it has been reported that a post sol-gel synthesis hydrothermal treatment resulted in the production of 6 and 10 nanometer titania nanocrystals at milder temperatures of 80°C and 180°C respectively<sup>70</sup>.

### 2.3.2 *Forced hydrolysis: hydrothermal/solvothermal synthesis*

At increasing temperatures, metal-coordinated water molecules will readily deprotonate to form metal hydroxide intermediates which condense to form M-O-M networks (e.g., TiO<sub>2</sub>). Thus, *forced hydrolysis* relies on the ease with which polyvalent metal (M) cations hydrolyze along with increasing temperature. Higher temperatures will increase the rate of hydrolysis and thus will result in a high degree of supersaturation of the hydroxylated metal cations<sup>71</sup>. The supersaturation condition within the system will induce nucleation, producing a large number of small nuclei.

Hydrothermal synthesis refers to the forced hydrolysis of crystalline materials in pressurized aqueous media above the boiling point of water. In order to reach the saturation vapor pressure, the reactions are carried out in Teflon-lined steel vessels called autoclaves<sup>72</sup>. The primary benefit of the hydrothermal method is the ability to obtain

crystalline product at lower reaction temperatures ( $< 250^{\circ}\text{C}$ ) than that required by sintering an amorphous material (for instance, via the sol-gel method<sup>73</sup>). Furthermore it has been shown that variation of system parameters such as pH, temperature, reaction time, etc. can be used to control the phase and size of the synthesized nanocrystals<sup>25</sup>.

The solvothermal method is similar to the hydrothermal method with the exception that the solvent used is nonaqueous. The solvothermal allows for a wider range of both pressures and precursors. Thus the solvothermal method has been demonstrated to allow a high degree of control with respect to crystal size<sup>9</sup> and shape<sup>74</sup>.

### 2.3.3 *Controlled Release of Hydroxide Ions – Urea Hydrolysis*

*Controlled release of hydroxide ions* into a metal oxide precursor solution provides a slow accumulation of hydroxylated monomers until supersaturation has been reached. Similar to forced hydrolysis, achieving supersaturation will result in a burst of nuclei. Controlled release differs from forced hydrolysis in that hydroxide ions are produced typically via decomposition of a reagent in solution rather than the change in solution chemistry due to increasing temperature. The accumulation of hydroxide ions in the system induces an increase in the pH<sup>75</sup>. This increase in pH means more  $\text{OH}^-$  ions will be produced and increase the probability of nucleophilic attack on the metals leading to hydrolysis. Subsequent condensation reactions will proceed as shown in equation 2.3.

Controlled release has been demonstrated using decomposition products of urea or formamide although direct vapor-diffusion of ammonia has also been used to produce

hydroxide ions to synthesize metal hydroxide, metal oxide, and metal phosphate thin films<sup>76</sup>. Decomposition of urea liberates ammonia molecules, which react with water to form ammonium hydroxide. This liberation of ammonia from urea results in an overall increase in pH of the system according to the following reaction mechanisms<sup>77</sup>.



Generally heat has been used as the means to decompose urea as it is known to decompose easily above 90°C. Thermal decomposition of urea has been used to produce aluminum basic sulfate<sup>78</sup>, cobalt (II) nitrate<sup>79</sup> as well as TiO<sub>2</sub><sup>80</sup>.

#### *2.4 Concluding remarks*

Titanium dioxide remains one of the most intensely studied materials for use in photocatalytic/photoelectrochemical applications. The reasons behind this are its photostability, natural abundance, and its environmentally benign nature. Synthesis of TiO<sub>2</sub> has been studied via a myriad of conditions, the majority of which require a high input of energy and/or the use of environmentally harsh solvents. In fact, the main drawback to industrial application of titanium dioxide for use in photocatalytic/photoelectrochemical applications is the high cost of nanocrystalline material with controlled size shape and phase. Thus, finding a low temperature and environmentally benign synthesis method would be advantageous.

## Chapter 3: Urease Mediated Synthesis of Titanium Dioxide

### 3.1 Lessons from nature

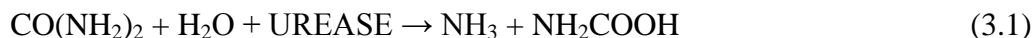
TiO<sub>2</sub> can be produced efficiently using a variety of methods, however, many of these require a substantial input of energy or the use of environmentally harsh materials. Over billions of years, evolutionary pressures have enabled nature to design highly selective strategies for designing materials on a molecular level. Bio-mediated approaches offer pathways to the production of large surface area, nanocrystalline materials under benign conditions such as room temperature, near-neutral pH, and in aqueous media<sup>81</sup>. At the heart of these bio-mediated approaches are biomacromolecules that are utilized either as biological constructs, which template the formation of a material, or as complex catalysts (i.e., enzymes) that drive a chemical reaction. Unlike traditional beaker and benchtop reactions, which use exogenous sources of reagents that often yield heterogeneities in products due to their uneven distribution in solution<sup>82</sup>, enzymes provide the precise control of a reaction by genetically controlled active sites. These active sites are critical in the biological world as their precise coordination at the angstrom level provides a low energy pathway to complete a reaction.

Biomacromolecules have been used in the past to synthesize metal oxides including ZnO<sup>83</sup>, Cu<sub>2</sub>O<sup>84</sup>, Ga<sub>2</sub>O<sub>3</sub><sup>85</sup>. Several biomacromolecular pathways have been explored in order to produce TiO<sub>2</sub> under physiological conditions. For instance, Sumerel *et al.* demonstrated templated synthesis of amorphous TiO<sub>2</sub> using the enzyme silicatein to catalyze the hydrolysis and subsequent polycondensation of the water-stable organic

titanium precursor, Titanium(IV) bis(ammonium lactato) dihydroxide<sup>86</sup> (TiBALDH). Kroger *et al.* produced hollow microspheres (20-50 $\mu$ M in diameter) consisting of crystalline rutile TiO<sub>2</sub> at ambient temperature and neutral pH using the sillafin rSilC<sup>87</sup>, while Luckarift *et al.* synthesized amorphous titania at room temperature using lysozymes<sup>88</sup>. Although the aforementioned methods generally employ direct templating or catalysis of the synthesized materials, similar bio-mediated reactions may also be used to accurately generate reagents, thus providing a controlled environment for synthesis.

The rapid hydrolysis and condensation of precursors will generally result in the formation of either amorphous or metastable structures<sup>89</sup>. A controlled and uniform evolution of embryonic nuclei can result in a homogenous size distribution among the synthesized nanomaterials<sup>90</sup>. Slow, uniform vapor diffusion of ammonia into a reaction medium<sup>91,92</sup> has generated metal oxide materials at room temperature due to the controlled condensation of hydrolyzed precursors, but with less control over size distribution. The uniform thermal decomposition of formamide<sup>93</sup> and urea at moderate temperatures<sup>94,95,96</sup> has yielded a homogenous evolution of solution pH to synthesize nanomaterials. This decomposition of urea, which occurs at temperatures in excess of 90°C, results in the liberation of ammonia molecules, which react with water to form ammonium hydroxide, which subsequently dissociates to form hydroxide ions. This discharge of ammonia from urea results in an overall increase in pH<sup>97</sup>.

Conversely, the decomposition of urea can also be achieved via enzymatic routes. In aqueous solutions, urease catalyzes the decomposition of urea according to the following reaction scheme:



The byproduct of reaction (3.2), carbonic acid, is further decomposed to carbon dioxide and water. The catalyzed reaction occurs  $10^{14}$  times faster than the un-catalyzed hydrolysis of urea, under ambient conditions<sup>98</sup>. Ureases such as those present in the cell wall of the bacteria *Helicobacter Pylori* (*H. Pylori*), the main cause of gastritis and peptic ulceration, use the enzyme to decompose urea present in the highly acidic environment of the stomach in order to provide a suitable environment (i.e., neutral pH) for reproduction of the cell<sup>99</sup>. In plant species, urease is used to augment the intake of nitrogen that may not be available from fixation for the nitrogen cycle. A commonly investigated urease is found in the Jack Bean plant (*Canavalia ensiformis*). Jack bean urease (JBU) is of historical significance as the first enzyme to be crystallized<sup>100</sup> as well as the first recognized nickel dependent metalloenzyme<sup>101</sup>. Urease from the Jack Bean plant consists of a hexameric structure (MW  $\approx$  480kD), figure 3.1a<sup>102</sup>, and a catalytic site consisting of Ni ions (fig. 3.1b)<sup>103</sup> that are precisely juxtapositioned to enable the hydrolysis of urea, yielding ammonia byproducts. One proposed mechanism of urease catalyzed decomposition is shown in figure 3.1c<sup>104</sup>.

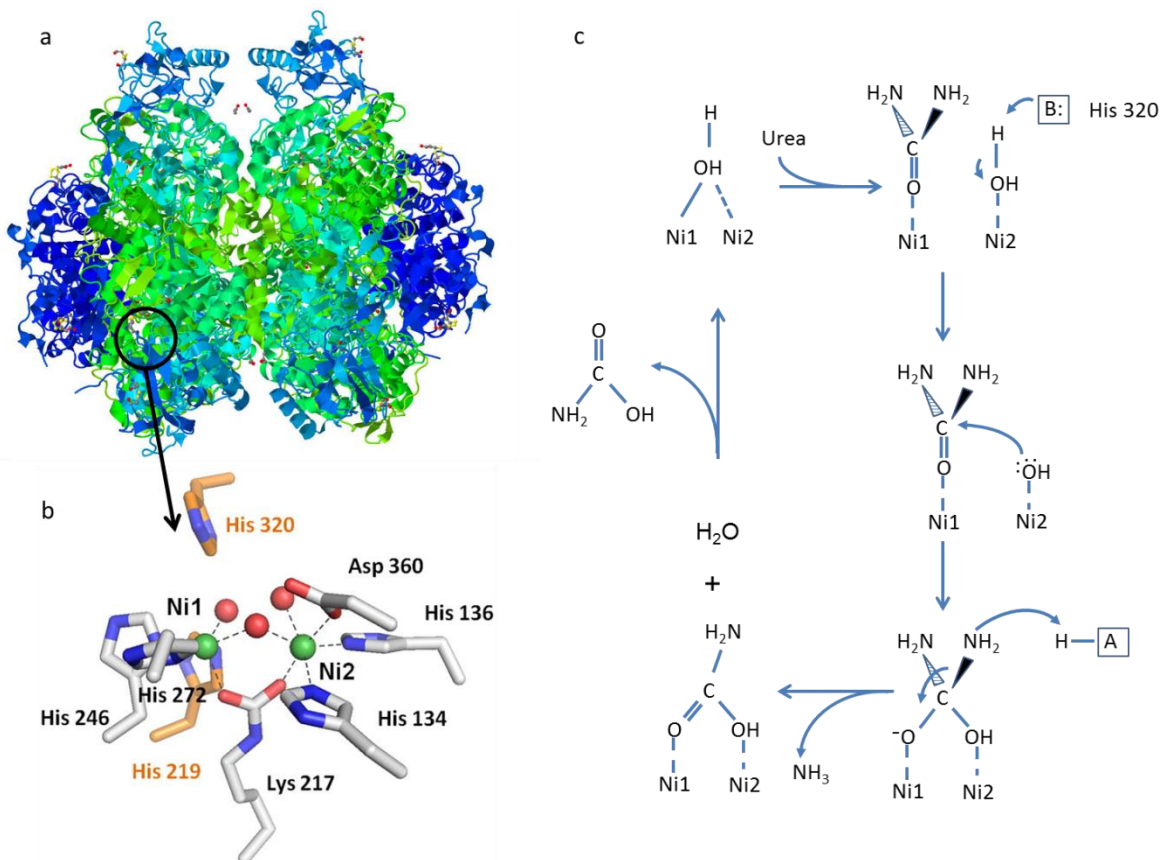


**Figure 3.1:** a) Hexameric structure of Jack Bean Urease (PDB# 3LA4), b) Jack Bean urease catalytic site, c) proposed mechanism for urea decomposition by urease.

The stability of a bidentate metal chelate titanium precursor, such as (TiBALDH), under ambient conditions is due to the interaction of adjacent oxygen and carboxylic functional groups<sup>105</sup>. This conjugate system allows for delocalization of electrons away from an oxygen molecule complexed to a central metal ion, resulting in a reduction of the Lewis basicity of the coordinated oxygen atom<sup>106</sup>. The homogenous dispersion of urease throughout the solution coincides with a homogenous increase in concentration of hydroxide ions ( $\text{OH}^-$ ). These nucleophilic ions hydrolyze the TiBALDH by simultaneous, nucleophilic attack of free hydroxide ions on the juxtaposed bidentate ligands coordinatively attached to a central  $\text{Ti}^{4+}$  ion<sup>107</sup> (fig. 3.2), leading to the formation of fully

(and partially) hydrolyzed species that can participate in condensation reactions. This is advantageous over adding an exogenous base in that even under rapid stirring, TiBALDH molecules located at the surface of the reaction media will react with hydroxide ions before those that are at the bottom of the reactor. In addition, the use of an enzyme to generate hydroxide ions circumvents the need to thermally decompose formamide or urea, and thus, the reaction can be sustained at room temperature which, enables the growth of these materials on polymeric substrates (e.g., electrically conductive polymers as electrodes for flexible sensitized solar cells).

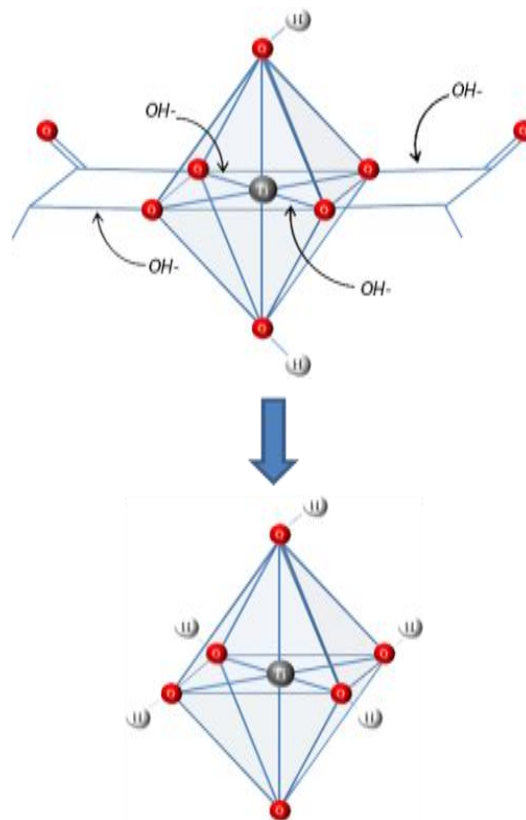


**Figure 3.2: Hydrolysis of titanium(IV) bis(ammonium lactato) dihydroxide by hydroxyl species present in solution.**

### 3.2 Experimental/Discussion

#### 3.2.1 General methods

**TiO<sub>2</sub> synthesis experiments and urease activity measurements:** As noted, Jack Bean Urease was purchased from Worthington Biochemical Corporation (MW = 480,000 Da, 45 units/mg). The enzyme arrived pre-dialyzed and lyophilized so no further purification was required. Urea powder and TiBALDH solution, 50 wt % in water were

purchased from Sigma-Aldrich. All solutions were prepared using nanopure water (Milli-Q). Post-synthesis the products were immediately removed and centrifuged at 4°C for 1hr at 16,000 rpm. Following removal of the supernatant, the pellet was re-suspended in nanopure H<sub>2</sub>O and sonicated (Branson 2510) for 30 minutes. The washing process was repeated four times to ensure complete removal of unreacted precursors and by-products. After the washing process the pellet was dried at 60°C for 24hrs. The dried products were ground to a fine powder and set aside for analysis.

**X-ray Diffraction (XRD):** A portion of the dried and ground powder were ground to a fine powder and placed on a glass microscope slide and characterized using X-ray diffraction (Philips X'Pert) with Cu K $\alpha$  radiation ( $\lambda = 1.540 \text{ \AA}$ ) over a range  $2\theta = 10^\circ - 70^\circ$ .

**Transmission Electron Microscopy (TEM):** Unless otherwise noted, Transmission Electron Microscopy (T-20 and Titan, FEI) was used to observe the lattice fringes of the as-synthesized TiO<sub>2</sub> nanomaterials and for size dispersion quantification. TEM specimens were prepared by dispersing the as-synthesized powder in ethanol, sonicating for 30 seconds (Hielscher, UP100H) and depositing the suspension onto 400 mesh holey-carbon copper grids (Ted Pella).

**Diffuse Reflectance:** Diffuse Reflectance spectra were measured using a Thermo-Scientific Evolution 300 UV-Vis Spectrophotometer with Praying Mantis Diffuse Reflectance attachment. The scan speed, bandwidth, and data interval were set to 240nm/min, 1nm, and 1nm respectively.

**Electron Dispersive Spectroscopy (EDS):** Elemental analysis was performed on the as-synthesized material using an XL30FEG Scanning Electron Microscope with integrated EDS system.

### 3.2.2 Urease activity: Michaelis-Menten analysis at varying temperatures

Quantitation of the enzymatic urease activity was performed using methodology a similar to that presented by Krajewska *et al.* in 2002<sup>108</sup>. Reaction solutions were prepared consisting of 0.01M TiBALDH and varying concentrations of urea (0.001, 0.002, 0.01, 0.02, 0.1, and 0.2M). Reactions were initiated by injection of 0.1mL, freshly prepared, 4.2 $\mu$ M aqueous urease suspension (final urease concentration of 0.013 $\mu$ M). An ammonium ion probe (Vernier) was connected a computer and the ammonium ion concentration was monitored and recorded every 5 seconds, in 5 minute intervals using Vernier LabPro software. These experiments were performed at 25°C, 40°C, and 60°C.

Reaction solutions were allowed to reach the expected experimental temperature prior to urease injection. All samples were prepared in sealed reaction vessels and magnetically stirred at 990rpm The initial rate data was used for subsequent Michaelis-Menten and Lineweaver-Burke analyses to determine the Michaelis constant and the maximum rate of ammonium ion production for each synthesis temperature.

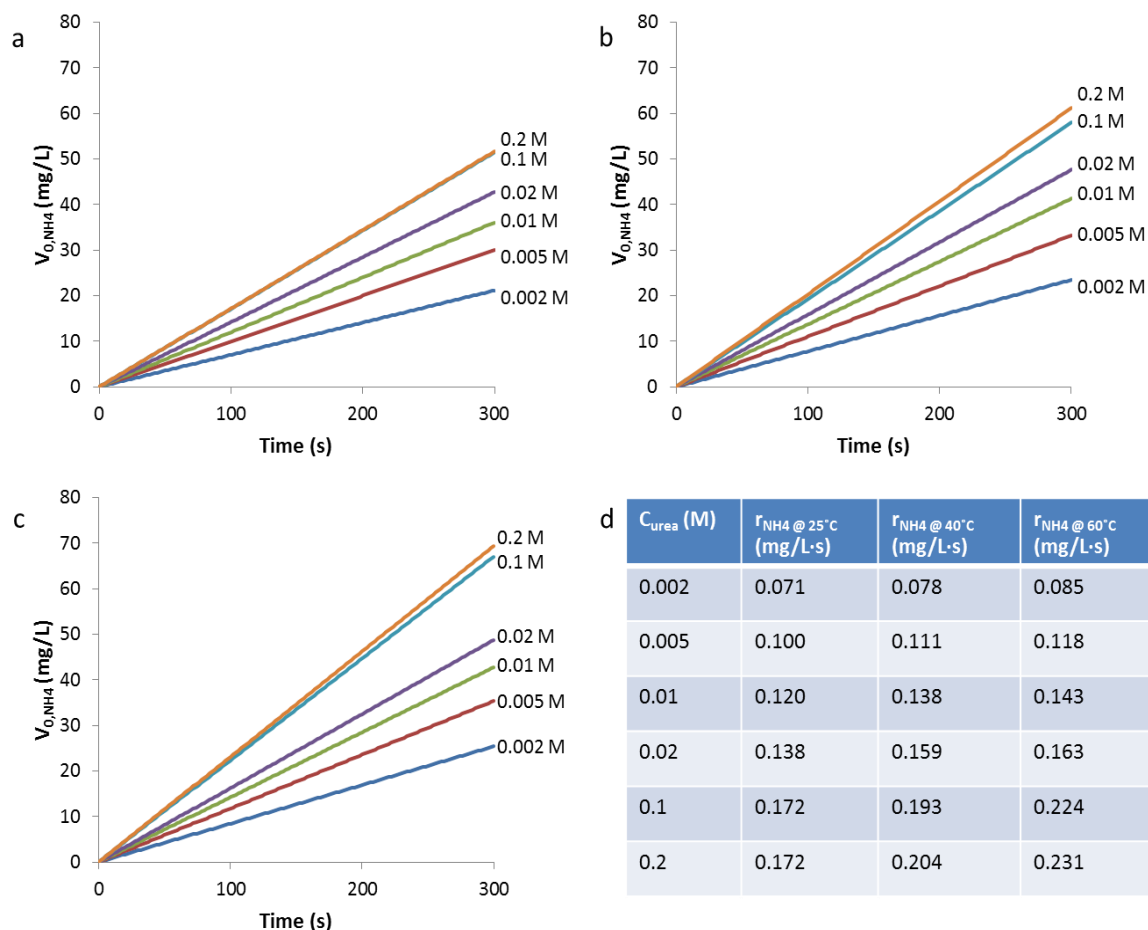
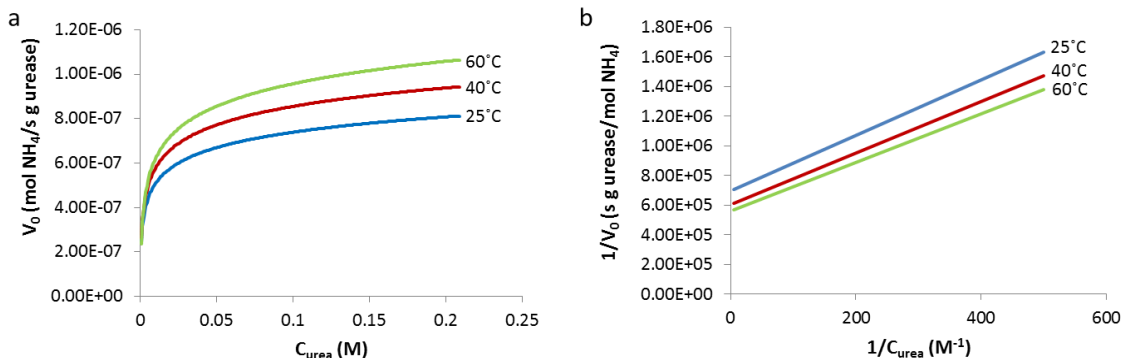


Figure 3.3: a), b), and c) are plots showing the change in ammonium ion concentration with respect to time for temperatures: 25, 40, and 60°C respectively, d) tabulated values of the rate of ammonium ion production with respect to time.

The initial rates of ammonium ion production due to urease catalyzed decomposition of urea, for varying concentrations of urea, are depicted in figures 3.3a – 3.3c for respective experimental temperatures of 25°C, 40°C, and 60°C. The collected initial rates (fig. 3.3d) were determined by taking the individual slopes of the curves representing the change in ammonium ion concentration over time. The plots show that for urea concentrations less than 0.1M, the rate of ammonium ion production increases with increasing urea concentration. For urea concentrations greater than 0.1M the rate of

ammonium production is constant, implying that all active sites are being utilized. The corresponding Michaelis-Menten curves (figure 3.4a) show that the activity of the enzyme increases with increasing temperature. The Michaelis constant  $K_M$  and the maximum reaction rate  $V_{max}$  were obtained by Lineweaver-Burke analysis (figure 3.4b) of the Michaelis-Menten curves. The calculated  $K_M$  values are 2.70mM, 2.90mM, and 2.94mM for the samples incubated at 25°C, 40°C, and 60°C, respectively. The corresponding calculated  $V_{max}$  values were  $1.44 \times 10^{-6}$ ,  $1.66 \times 10^{-6}$ , and  $1.79 \times 10^{-6}$  mol of  $\text{NH}_4^+$  produced per second per mmole of enzyme. The Lineweaver-Burke analysis shows



**Figure 3.4:** a) Michaelis-Menten curves for urease mediated  $\text{TiO}_2$  synthesis solutions at 25°C, 40°C, and 60°C, b) Lineweaver-Burke plots for ammonium ion production in urease mediated  $\text{TiO}_2$  synthesis solutions at 25°C, 40°C, and 60°C.

that the maximum rate of ammonium ion production increases with increasing temperature, similar trends have been shown in previous studies<sup>109,110</sup>. It is well known that most enzyme catalyzed reactions initially follow an Arrhenius-type rate dependence whereby the reaction rate increases linearly with increasing temperature due to an increase in kinetic energy of the reactants which, increases the probability that a substrate molecule will collide with an active site on the enzyme. The Arrhenius rate dependence

continues until the enzyme begins to thermally denature, changing its molecular conformation and deactivating sites.

### *3.2.3 Urease Mediated Synthesis of TiO<sub>2</sub>*

Initial “proof-of-concept” experiments were performed to determine if TiO<sub>2</sub> could be produced using the urease mediated method. A 30mL reaction sample was prepared in an aqueous solution composed of 0.1M TiBALDH and 0.33M Urea. The urease used in these initial experiments was purchased from Sigma-Aldrich (lyophilized powder, ~100 U/mg, 480kDa). The enzyme was dialyzed using Spectrum Spectra/Por Biotech Regenerated Cellulose (RC) Dialysis Membranes, MWCO: 3500. Dialysis was carried out in 8L of nanopure water over 36 hours with water changes every 6 hours. The dialyzed enzyme was then lyophilized and the resulting material stored at -20°C prior to use. The reaction temperature was 60°C. Reactions were initiated by injection of 1mL, freshly prepared, 3.9µM aqueous urease suspension (concentration = 0.13µM).

By way of controls two additional reaction solutions were prepared as above (0.1M TiBALDH, 0.33M Urea, preheated to 60°C). To the first control solution 1mL of aqueous urease suspension, heat denatured by incubation in nanopure H<sub>2</sub>O, at 90°C for 25 minutes, was injected as the reaction initiator. The second control solution was injected with Bovine Serum Albumin (Sigma-Aldrich, lyophilized powder) to a concentration of 0.13 µM. Reactions were carried out in capped glass vials under magnetic stirring at 700rpm over a period of 24 hours. The experimental sample became slightly opaque within the first hour of the experiment, indicating the presence of

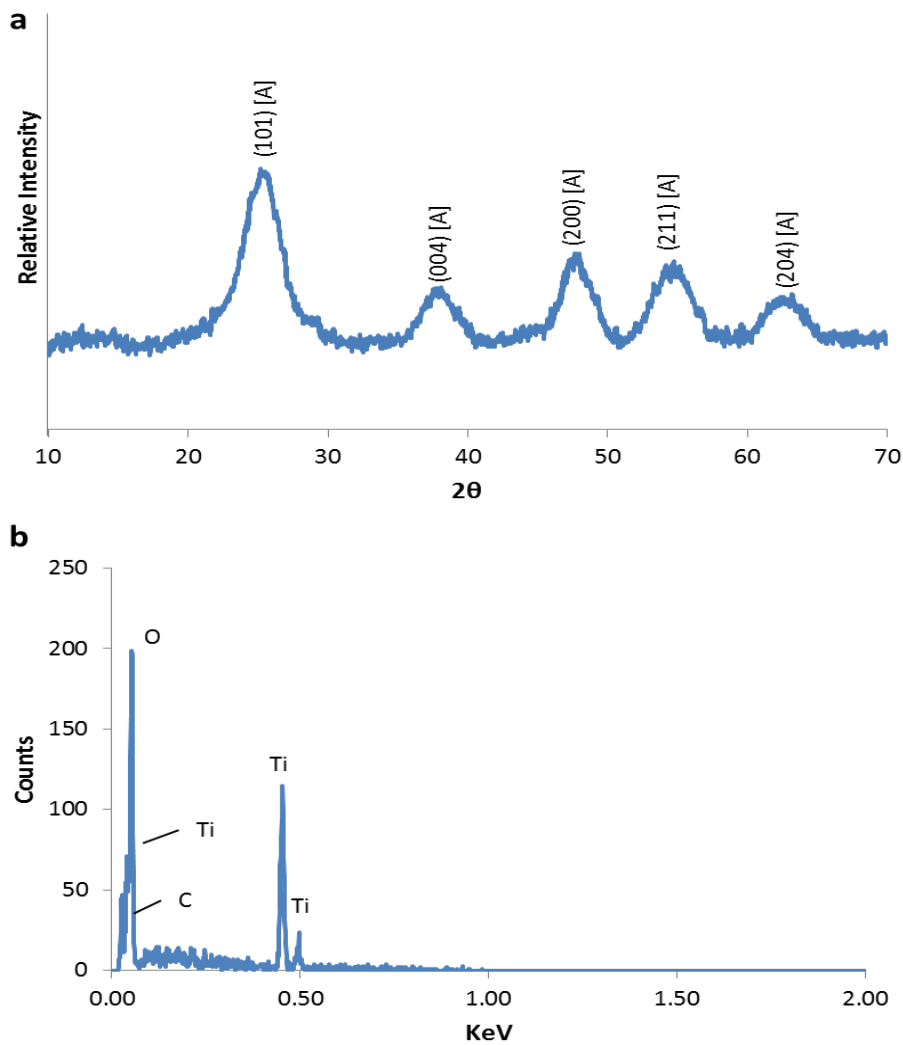


**Figure 3.5: XRD pattern (a) and EDS spectrum (b) of the as-synthesized materials showing the presence of  $\text{TiO}_2$ .**

precipitate; the heat denatured urease and BSA controls did not show precipitate at any time over the 24 hour reaction period. After the allotted reaction time, the precipitating reaction solution was immediately removed and centrifuged at 4°C for 1hr at 16,000 rpm. Following removal of the supernatant, the pellet was re-suspended in nanopure  $\text{H}_2\text{O}$  and sonicated (Branson 2510) for 30 minutes. The washing process was repeated four times

to ensure complete removal of unreacted precursors and by-products. After the washing process the pellet was dried at 60°C for 24hrs.

The final pHs of the reaction solutions were 9.21, 7.81, and 7.14 for the native urease, heat-denatured urease and BSA injected samples, respectively. The low solution pH of the non-precipitating controls indicates that the concentration of OH<sup>-</sup> ions, and therefore the amount of hydrolyzed TiBALDH molecules, did not reach a point of supersaturation, and thus no nucleation event occurred.

The X-ray diffractogram representing the urease catalyzed TiO<sub>2</sub> (fig. 3.5a) shows reflections at  $2\theta = 25.3^\circ$ ,  $37.8^\circ$ ,  $48.1^\circ$  and  $53.9^\circ$ , which correspond to the (101), (004), (200), and (105) reflections respectively (JCPDS # 01-084-1286), thus the samples appear to be composed primarily of crystalline anatase TiO<sub>2</sub>. The presence of a slight shoulder at  $2\theta = 27.4^\circ$ , as well as a minor peak at  $2\theta = 44.0^\circ$ , may indicate the presence of rutile (110) and (210) TiO<sub>2</sub> respectively (JCDPDS#01-073-1765) but subsequent analysis by TEM did not corroborate this. EDS (fig. 3.5b) was used for elemental analysis of the as-synthesized material showing a structure predominantly composed of titanium and oxide with a small quantity if residual carbon possibly present from residual precursor or enzyme that was not removed during the washing process. The success of the initial 60°C experiments prompted further experiments at decreasing temperatures.

### 3.2.4 Urease mediated synthesis of $\text{TiO}_2$ : temperature study

All reaction solutions consisted of 0.1M TiBALDH and 0.33M urea prepared in 30mL nanopure water (Milli-Q). Synthesis of nanocrystalline  $\text{TiO}_2$  was carried out at three different temperatures 25°C, 40°C, and 60°C. Reaction vessels were incubated in a water bath at the appropriate temperature. All solutions were allowed to reach the expected experimental temperature prior to initiation of the urease catalyzed reaction. Reactions were initiated by injection of 1mL, freshly prepared, 3.9 $\mu\text{M}$  aqueous urease suspension (for a reaction concentration of 0.13 $\mu\text{M}$  with respect to urease). Reactions were carried out in capped glass vials under magnetic stirring at 700rpm. The reaction time was 36 hours, after which, the products were immediately removed, washed and dried. The dried products were ground to a fine powder and set aside for analysis.

XRD analysis of the as-synthesized materials (Figure 3.6a) uncovered reflections at  $2\theta = 25.3^\circ$ ,  $37.8^\circ$ ,  $48.1^\circ$  and  $53.9^\circ$ , which correspond to the (101), (004), (200), and (105) planes, respectively, of anatase  $\text{TiO}_2$  (JCPDS # 01-084-1286). Scherer analysis of the (200) reflection<sup>111</sup> was used to calculate crystal diameters of  $\text{TiO}_2$  synthesized at 25°C, 40°C, and 60°C for 36 hours (Figure 3.6b). It is clear that the average  $\text{TiO}_2$  crystallite size remains nearly constant, at or near 3.0 nm, under these reaction conditions. In addition to the anatase reflections, two minor peaks observed  $27.4^\circ$  and  $44.0^\circ$  may indicate the presence of rutile  $\text{TiO}_2$  (JCDPDS#01-073-1765). However, further evaluation is necessary to confirm this.

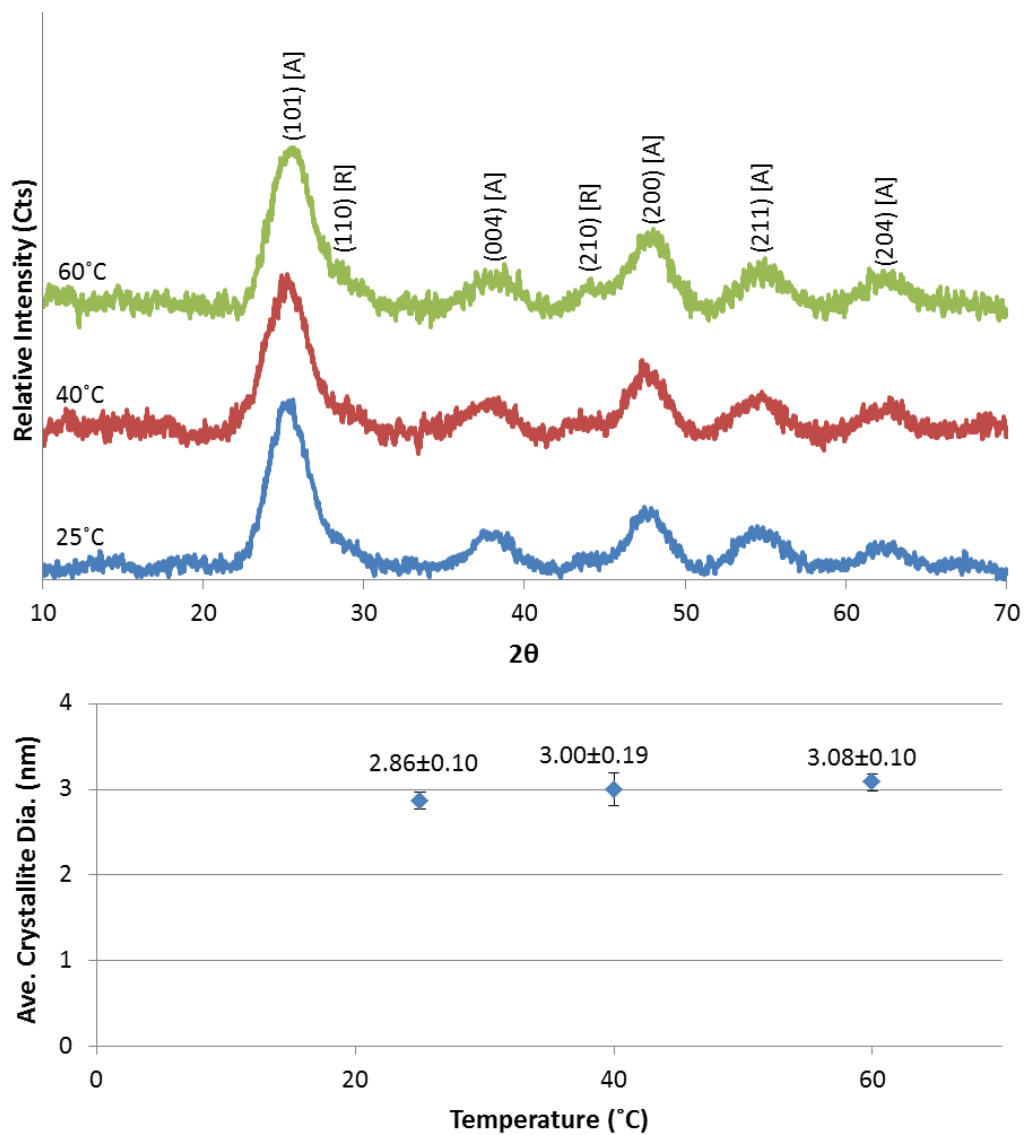


Figure 3.6: XRD patterns for materials synthesized via the urease mediated method at temperatures of 25°C, 40°C, and 60°C, and b) corresponding plots showing the variation in crystallite size for the experimental temperatures.

In order to confirm the size and phase of the as-synthesized materials, samples were imaged using TEM (i.e., bright field imaging and selected area electron diffraction).

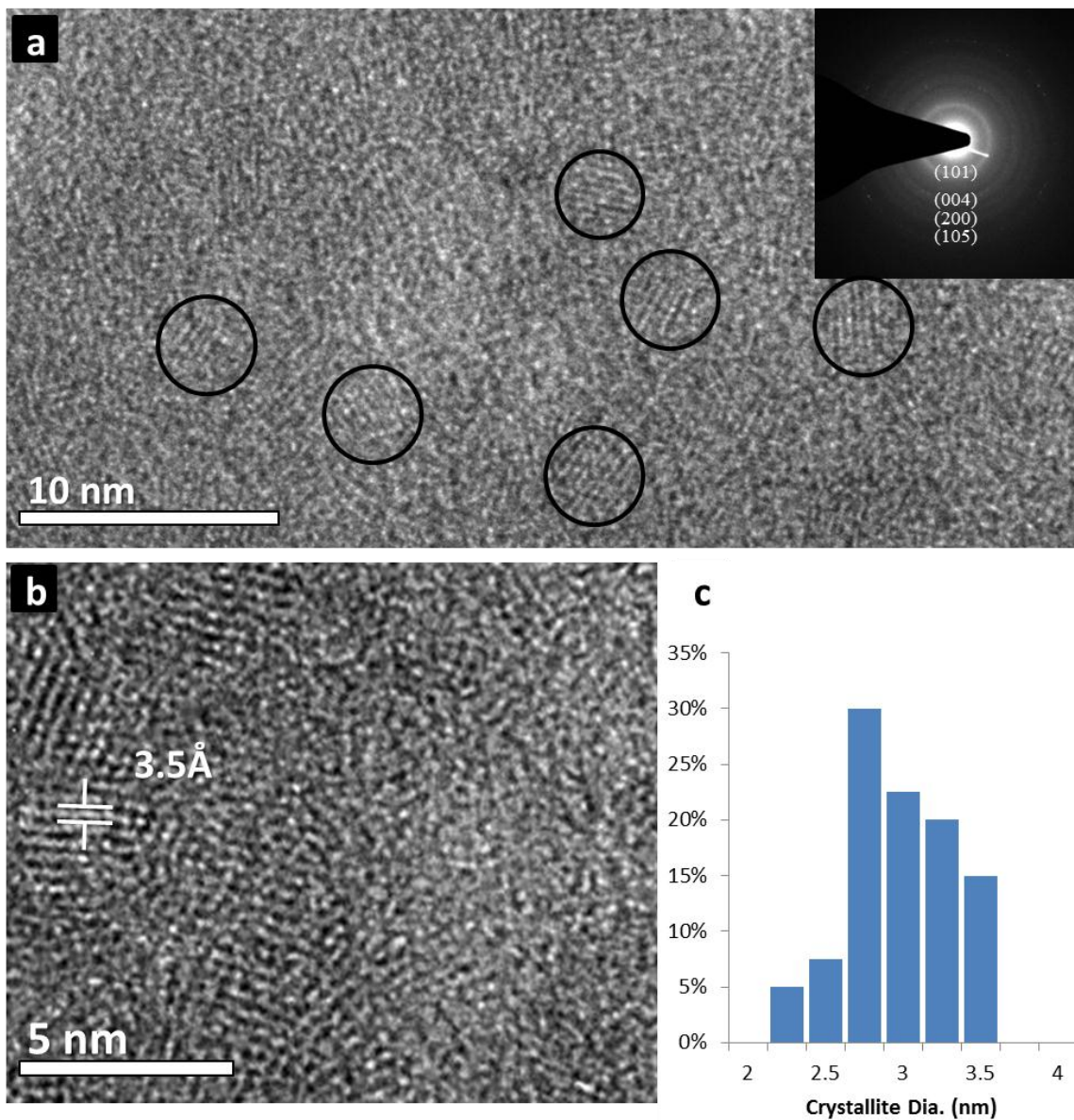


Figure 3.7: Bright field TEM image, with SAED inset (a), HRTEM image (b), and representative histogram (c) of  $\text{TiO}_2$  synthesized at 25°C for 36hours, the circles indicate apparent lattice fringes.

TEM images for samples prepared at 25°C, 40°C and 60°C for 36 hours are presented in

Figures 3.7a, 3.8a, and 3.9a, respectively, with insets showing corresponding selected

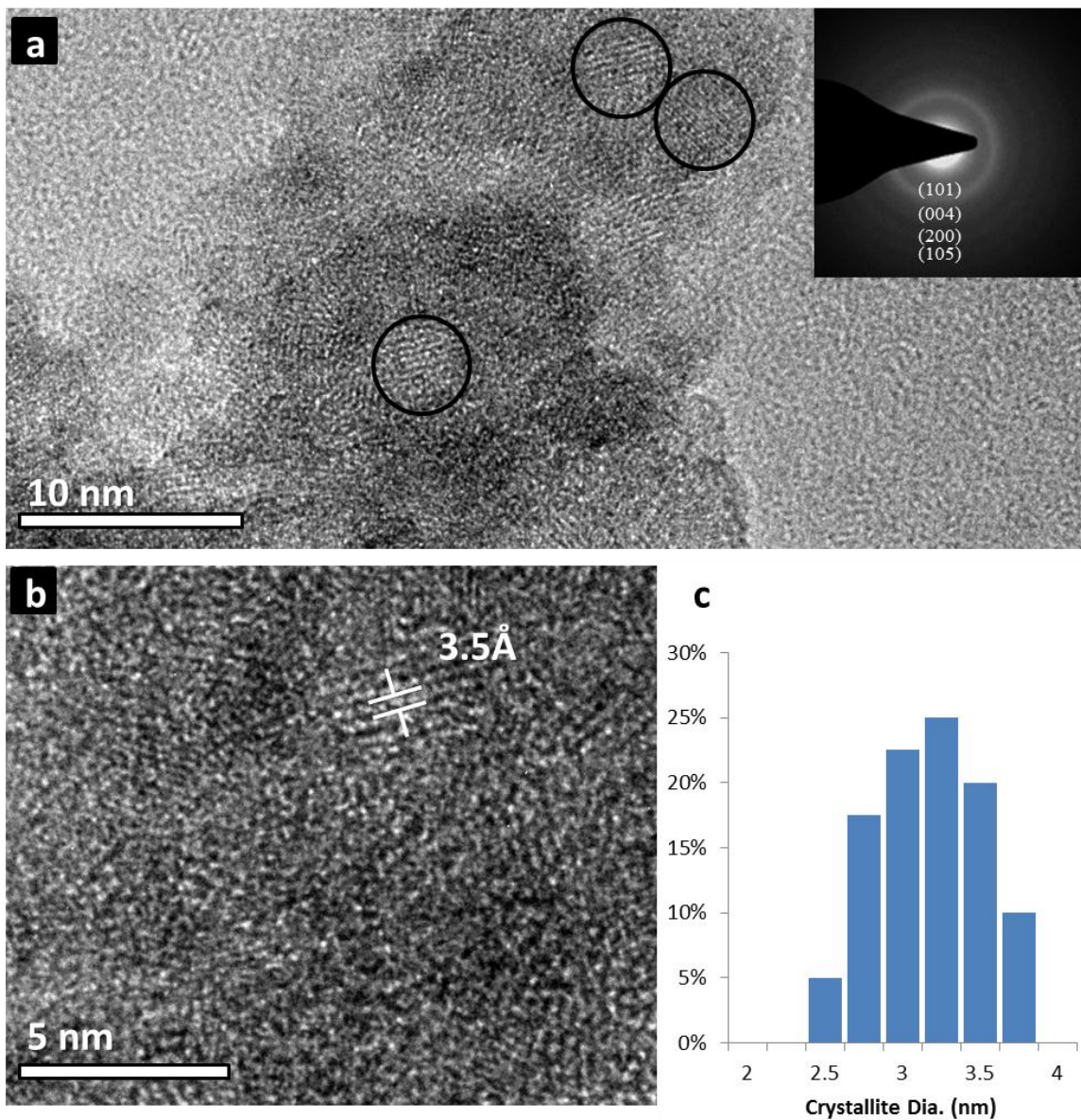


Figure 3.8: Bright field TEM image, with SAED inset (a), HRTEM image (b), and representative histogram (c) of TiO<sub>2</sub> synthesized at 40°C for 36 hours, the circles indicate apparent lattice fringes.

area diffraction (SAED) patterns of each specimen confirming the presence of nanocrystalline anatase TiO<sub>2</sub>. High-resolution bright field imaging of samples prepared at 25°C, 40°C and 60°C for 36 hours (Figures 3.7b, 3.8b, and 3.9b, respectively) all

demonstrate similar crystallite diameter (ca.  $\sim 3$  nm). Lattice imaging also confirmed anatase  $\text{TiO}_2$ , with d-spacings of the nanocrystals measuring ca.  $3.51 \pm 0.2\text{\AA}$  ((101)

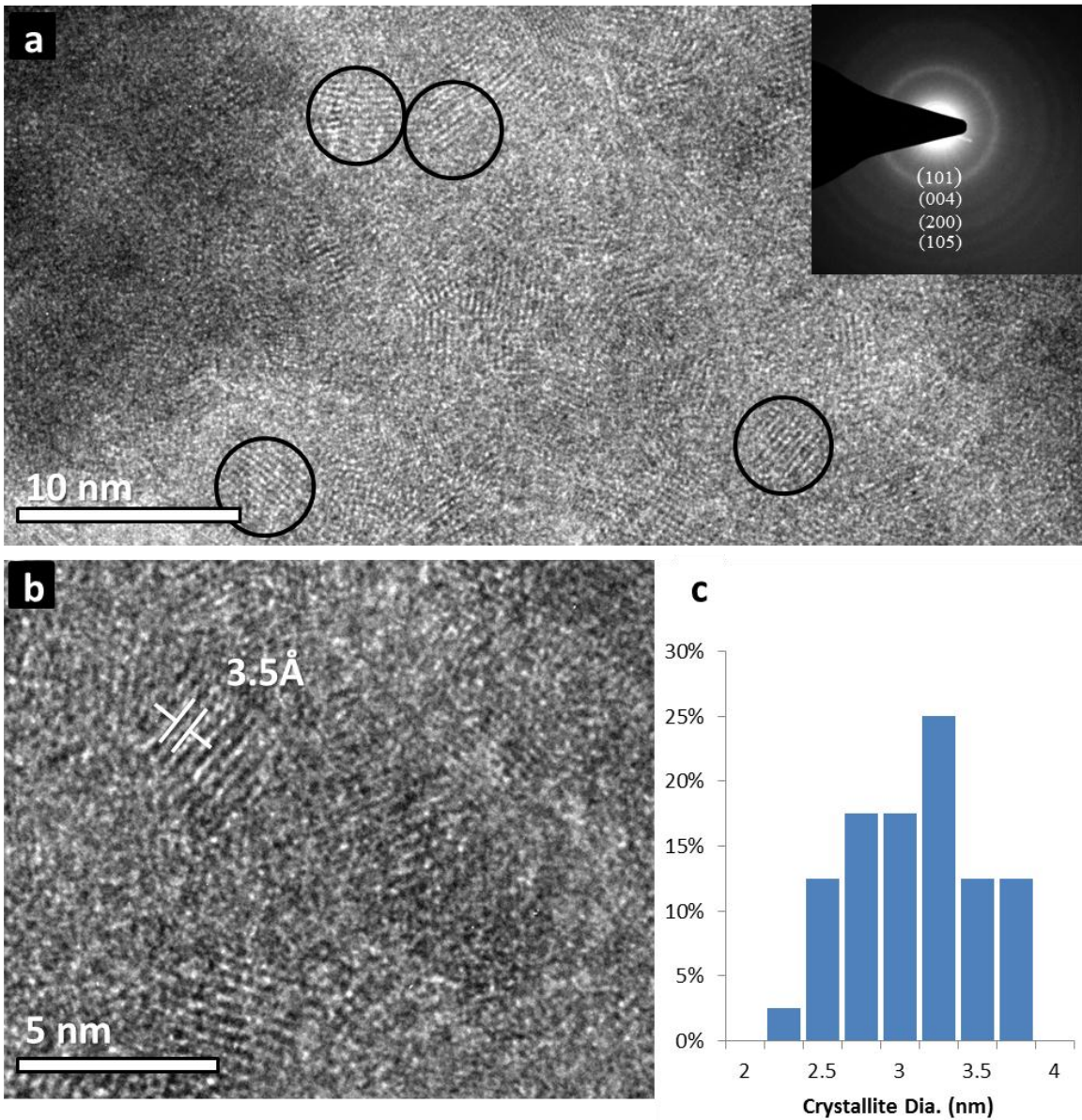
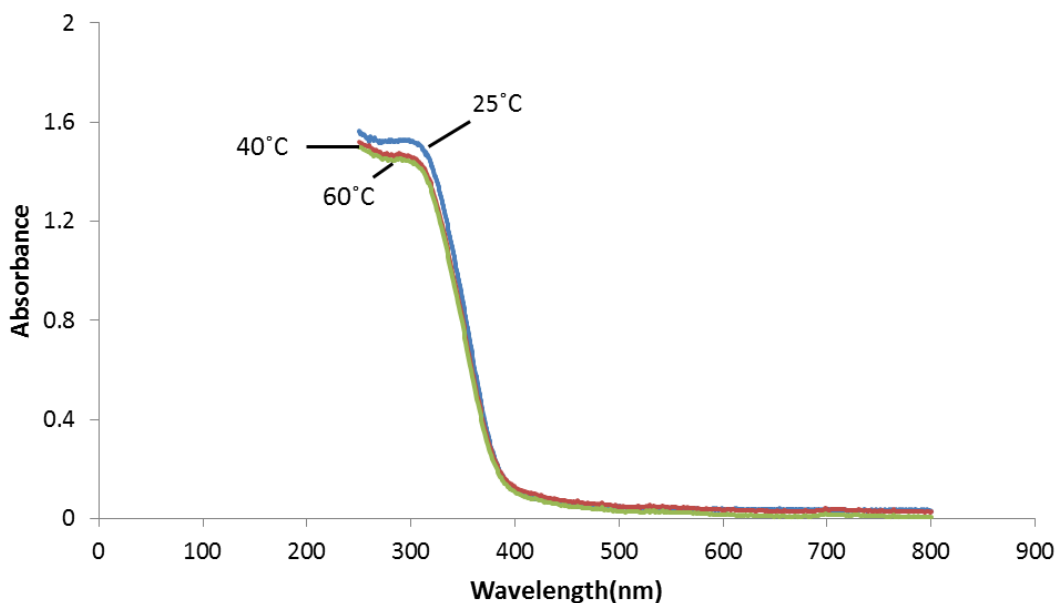


Figure 3.9: Bright field TEM image, with SAED inset (a), HRTEM image (b), and representative histogram (c) of  $\text{TiO}_2$  synthesized at  $60^\circ\text{C}$  for 36 hours, the circles indicate apparent lattice fringes.

anatase). Histograms representing the size dispersion found in the as-synthesized materials prepared at  $25^\circ\text{C}$ ,  $40^\circ\text{C}$  and  $60^\circ\text{C}$  for 36 hours (fig. 3.7c, 3.8c, and 3.9c) show

nanocrystal size indices of  $2.84 \pm 0.33$ ,  $3.03 \pm 0.31$ , and  $2.94 \pm 0.40$  respectively. Each histogram represents a count of 40 crystallites.

UV-Visible spectra (Figure 3.10) were also obtained for  $\text{TiO}_2$  synthesized at  $25^\circ\text{C}$ ,  $40^\circ\text{C}$ , and  $60^\circ\text{C}$  for 36 hours. The band gap measurements from this data were determined to be  $3.22\text{eV}$ ,  $3.21\text{eV}$ , and  $3.19\text{eV}$  for samples prepared for 36 hours at  $25^\circ\text{C}$ ,  $40^\circ\text{C}$ , and  $60^\circ\text{C}$ , respectively. Although there is a slight decrease in the observed band



**Figure 3.10:** Diffuse Reflectance spectra of urease synthesized  $\text{TiO}_2$  prepared at  $25^\circ\text{C}$ ,  $40^\circ\text{C}$ , and  $60^\circ\text{C}$  for 36 hours.

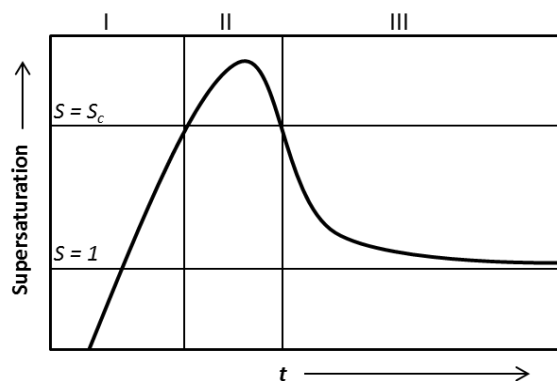
gap with increasing synthesis temperature, the results are within the margin of error and are therefore considered constant.

The measured band gaps are also similar to those observed in previous investigations<sup>112</sup> and reflect the predicted bandgap for anatase  $\text{TiO}_2$ . It has been demonstrated that the band-gap of nanocrystalline materials is affected by the nanocrystal

size<sup>113</sup>, whereby the band-gap increases with decreasing crystal size<sup>114</sup>. Thus, the near constant value with respect to the band gap further substantiates that the crystal size is constant irrespective of synthesis temperature, within the experimental temperatures studied.

Classical nucleation theory can be visualized using the well-established La Mer diagram shown in figure 3.11. It is theorized that in stage I, the minimum subunit of nucleation (monomers) are constantly forming larger particles which then subsequently decompose due to a large interfacial

surface energy. The high interfacial energy is due to the large surface area to volume ratios of these small particles, which contain a high fraction of unsaturated bonds. In stage II, the degree



of saturation ( $S$ ) has increased to a point greater than the critical supersaturation, and thus the interfacial energy barrier has been overcome and nucleation from the embryonic clusters occurs. At this point the monomer is being consumed at a rate greater than it is being supplied and hence the monomer concentration (and thus the supersaturation) falls until net nucleation has ceased. In stage III, net nucleation has completely stopped and the growth stage is initiated. This growth stage will continue as long as the solution maintains supersaturation ( $S > 1$ ).

**Figure 3.11: La Mer diagram illustrating the three phases of crystal nucleation**

Nucleation is governed by the total change in free energy for the system. Two competing factors determine at what point nucleation occurs. The surface free energy,

$$\Delta\mu_s = 4\pi r^2 \gamma \quad (3.3)$$

where,  $r$  is the cluster radius and  $\gamma$  is the surface energy per unit energy, and the energy gain provided by the creation of a new volume,

$$\Delta\mu_v = \frac{4}{3}\pi r^3 \Delta G_v \quad (3.4)$$

where,  $G_v$  is the change of Gibbs free energy per unit volume and is given by,

$$\Delta G_v = -\frac{\kappa T}{V_m} \ln(S) \quad (3.5)$$

where,  $\kappa$  is the Boltzmann constant  $1.806503 \times 10^{-23} \text{ m}^2 \text{ kg s}^{-2}$ ,  $T$  is the temperature,  $V_m$  is the atomic volume and  $S$  is the degree of supersaturation. The total change in energy for the system is the summation of the change in surface free energy and the change in Gibbs free energy per unit volume.

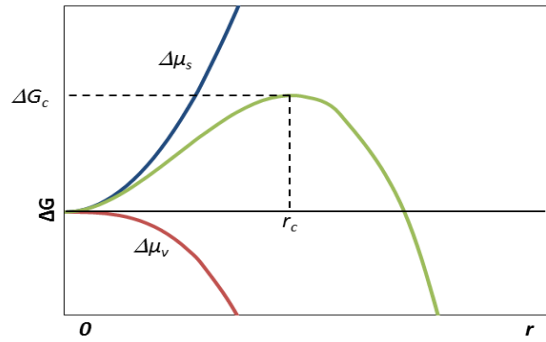
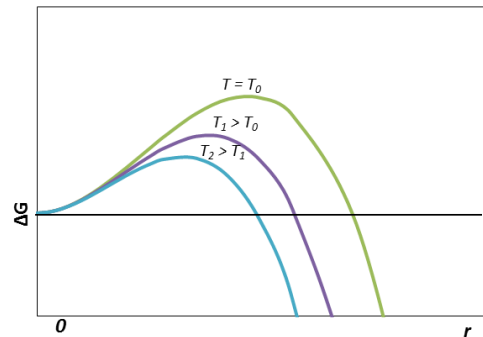


Figure 3.12: Plots showing the change in Gibbs free energy with respect to crystallite radius.

$$\Delta G = 4\pi r^2 - \frac{4\pi r^3 \kappa T}{3V_m} \ln(S) \quad (3.6)$$

From this equation, it can be seen that until the point of critical supersaturation is reached ( $S > S_c$ ) the energy barrier for nucleation will be insurmountable. For conditions of supersaturation, the effect is shown in a plot of Gibbs free energy versus crystallite radius (fig. 3.12). As the radius of the clusters increase, the surface area to volume ratio decreases. Under these conditions there are a greater number of internal bonds within the cluster volume versus available (unsaturated) bonds at the interface. Thus, there is a decreasing of the interfacial energy at the surface. When the critical radius ( $r_c$ ) is reached, where the critical energy ( $\Delta G$ ) has been overcome, stable nuclei will form. Clusters with a radius less than  $r_c$  will dissolve into solution providing monomers for subsequent growth of nanocrystals

Based on eqn. 3.6, it is apparent that there is a correlation between nanocrystal size and the temperature of the solution. This relationship is shown graphically (fig. 3.13), whereby the critical radius of nucleating crystallites decreases with increasing temperature. This is due to the increase in thermal energy reducing the overall critical energy required to surmount the interfacial energy barrier.



**Figure 3.13: Plots showing the effect of temperature on the Gibbs free energy of the solution.**

Crystallite growth may occur via two separate growth mechanisms, or a combination of both. The first mechanism, described by Ostwald in 1896<sup>115</sup>, referred to

as Ostwald ripening (OR), is based on a driving force, whereby larger crystals are more thermodynamically favored due to their smaller surface area to volume ratio. The smaller crystallites will have fewer stabilized interior bonds and more unsaturated surface bonds and will thus tend to dissociate under strain from interfacial tension. The smaller crystallites will subsequently act as nutrients for the growth of larger crystallites. OR typically occurs when there is a sufficient solubility of the material. The second mechanism that may occur when the solubility is low is oriented attachment (OA). In order to minimize surface energy, the highest energy faces will join with the highest energy faces of nearby crystals thus lowering the overall surface energy of the crystals<sup>116</sup>.

Since the initial sets of experiments did not appear to present a noticeable change in crystal diameter (within the experimental error), a subsequent set of experiments were carried out at elevated temperatures to determine if crystal growth may occur. The reaction solutions (0.1M TiBALDH, 0.33M urea, and 0.13 $\mu$ M urease) were initially run for 12 hours at 60°C in sealed glass reactors. These conditions would facilitate the production of the nanocrystalline TiO<sub>2</sub> without subjecting the enzyme to the denaturation effects of the higher temperatures. After the initial 12 hour synthesis, each reactor was removed to a separate 60°, 80°C, or 100°C oil bath and incubated for an additional 36 hours. Analysis of the XRD pattern (fig. 3.14a) demonstrates that the particle size remains constant at temperatures up to 80°C but there is an increase in the average crystal diameter at 100°C reaction conditions (fig 3.14b).

A similar experiment was presented by Finnegan in 2008, where initially prepared nanocrystals of 3.5nm TiO<sub>2</sub> were synthesized using the sol-gel method. These 3.5nm

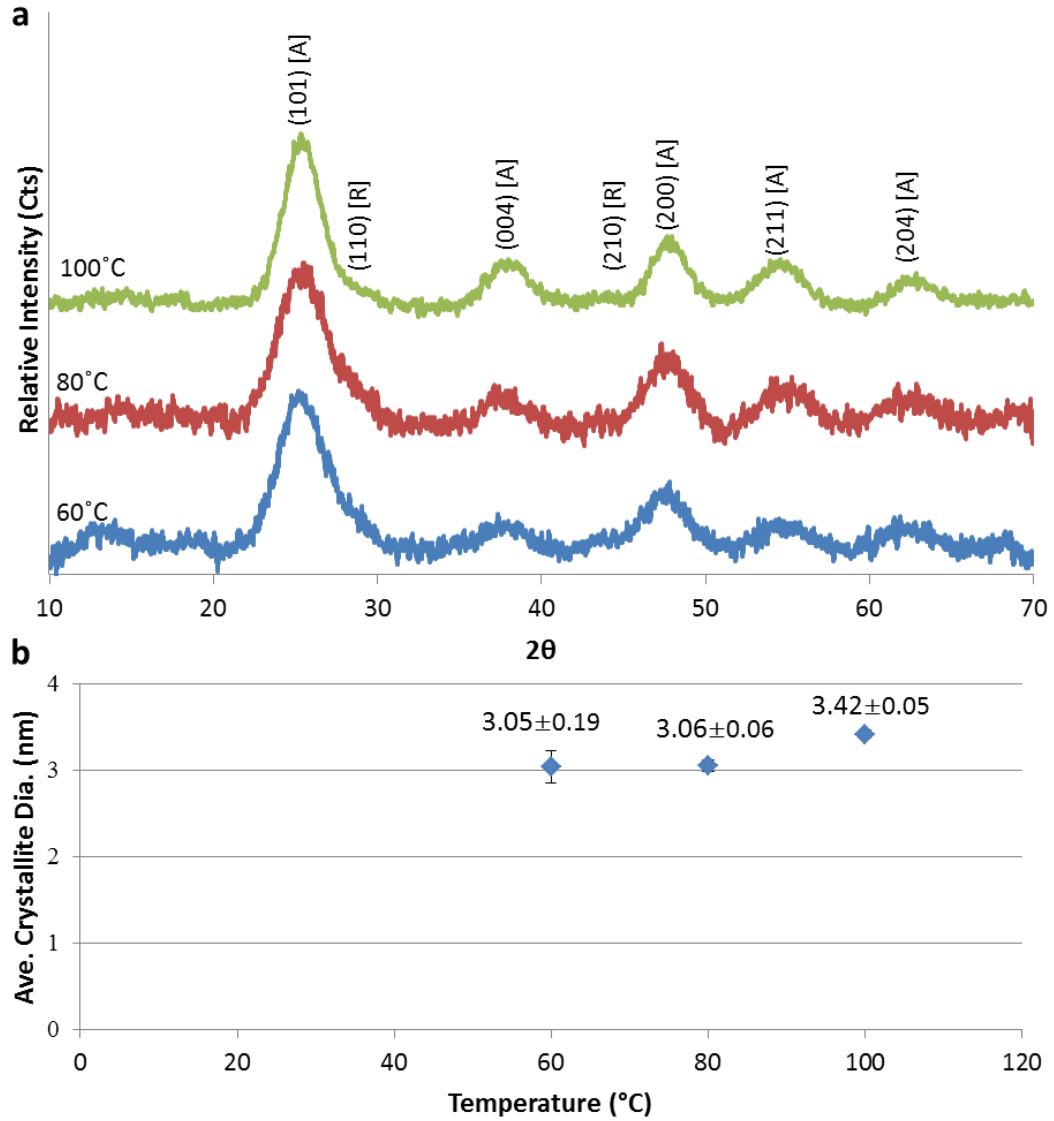


Figure 3.14: XRD patterns for materials synthesized via the urease mediated method at temperatures of 60°C, 80°C, and 100°C, and b) corresponding plots showing the variation in crystallite size for the experimental temperatures.

TiO<sub>2</sub> crystals were subsequently placed in an aqueous solution (pH = 8) and coarsened under hydrothermal condition (105°C) for up to 600 hours. Specimens treated in this way

showed an increase in crystallite size, growing from 3.5nm to 5.5nm<sup>117</sup>. Classical nucleation theory shows that crystal growth will occur, as long as a condition of supersaturation exists, and that the size of nucleating crystals is dependent on the temperature of the reaction solution. Based on the presented data presented herein, it appears that there is a size limitation imposed on the as-synthesized materials prepared at temperatures < 100°C. The possible reasons for this limitation will be addressed further in the concluding discussion section of this chapter.

### *3.2.5 Urease Mediated Synthesis of TiO<sub>2</sub>: Room Temperature Time Study*

Generally, for reactions carried out at 25°C, synthesis times of at least 12 hours were required in order to produce enough material for characterization via XRD. Thus, for the initial room temperature time study, the synthesis of nanocrystalline TiO<sub>2</sub> was carried out in time intervals of 12, 24, and 36 hours. Synthesis solutions were prepared similarly to those used in the temperature study (i.e., 0.1M TiBALDH, 0.33M urea, and 0.13μM urease), followed by washing and drying in the manner already detailed (i.e., centrifugation at 4°C for 1hr at 16,000 rpm with sonication for 30 minutes between centrifugations, and drying for 24 hours at 60°C).

The XRD patterns for the 12, 24, and 36 hour synthesis (fig. 3.15a) show patterns

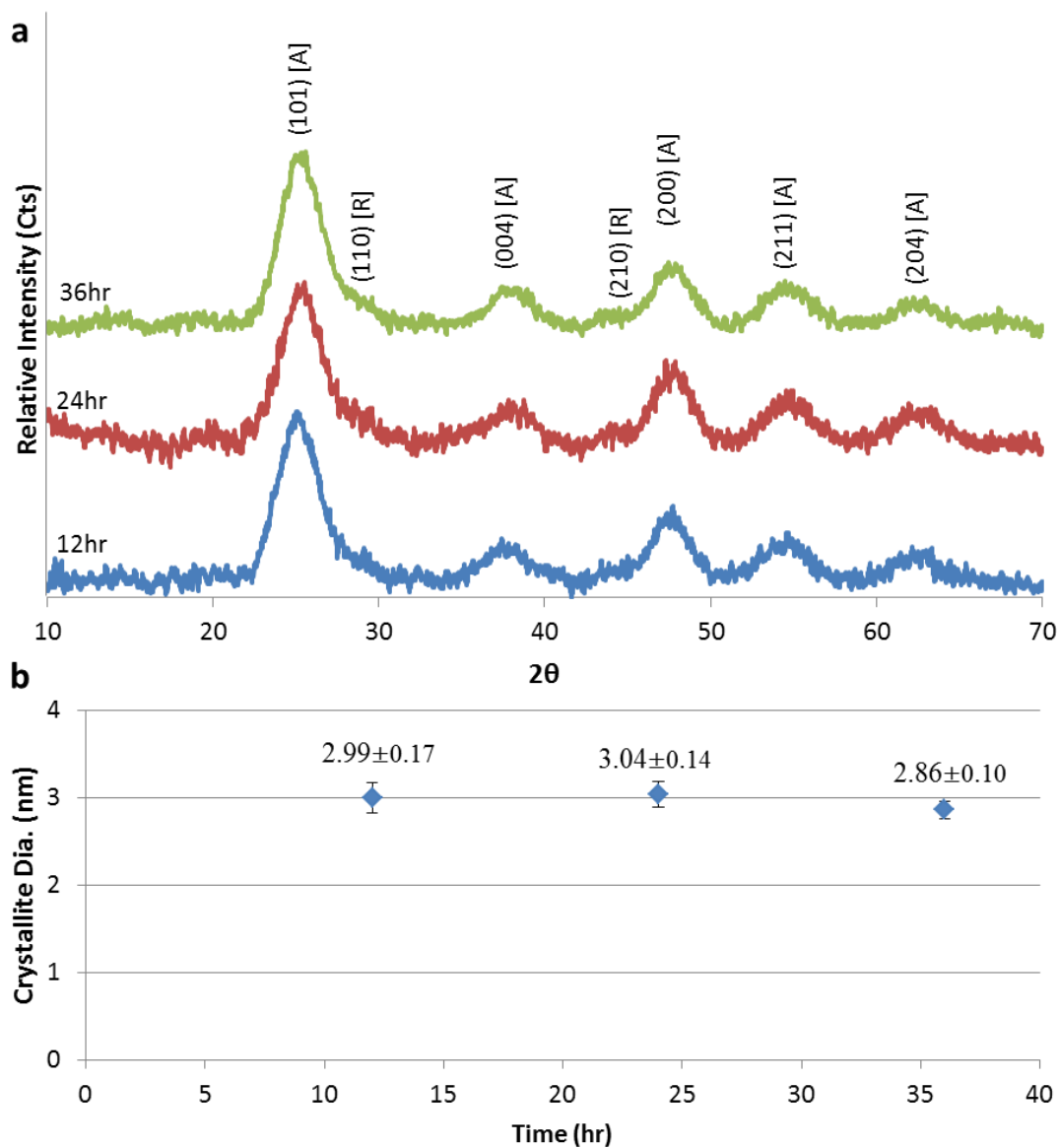


**Figure 3.15:** XRD patterns for materials synthesized via the urease mediated method at 25°C, for 12, 24, and 36hrs, and b) corresponding plots showing the variation in crystallite size for the experimental intervals.

indicative of anatase TiO<sub>2</sub> (i.e., 2θ = 25.3°, 37.8°, 48.1° and 53.9°), corresponding to the (101), (004), (200), and (105) planes as well as the minor peaks at 2θ = 27.4° and 44.0°,

observed previously, indicating the presence of rutile  $\text{TiO}_2$ . The plot depicting the change

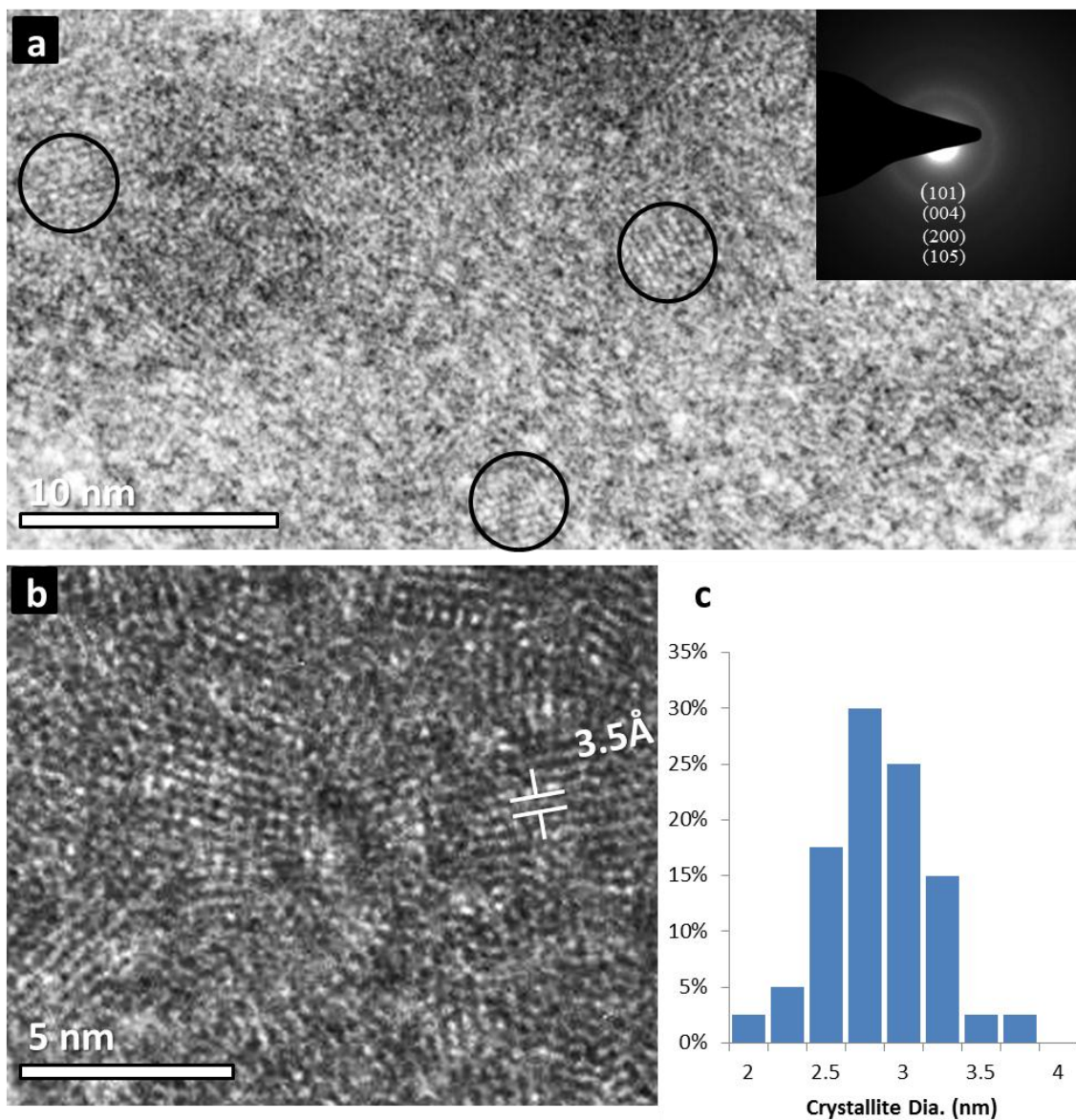


**Figure 3.16:** Bright field TEM image, with SAED inset (a), HRTEM image (b), and representative histogram (c) of  $\text{TiO}_2$  synthesized at  $25^\circ\text{C}$  for 12 hours, the circles indicate apparent lattice fringes.

in crystallite size with respect to reaction time (fig. 3.15b) shows nearly constant crystallite sizes regardless of the reaction times. TEM images (figs. 3.16a – 3.18a)

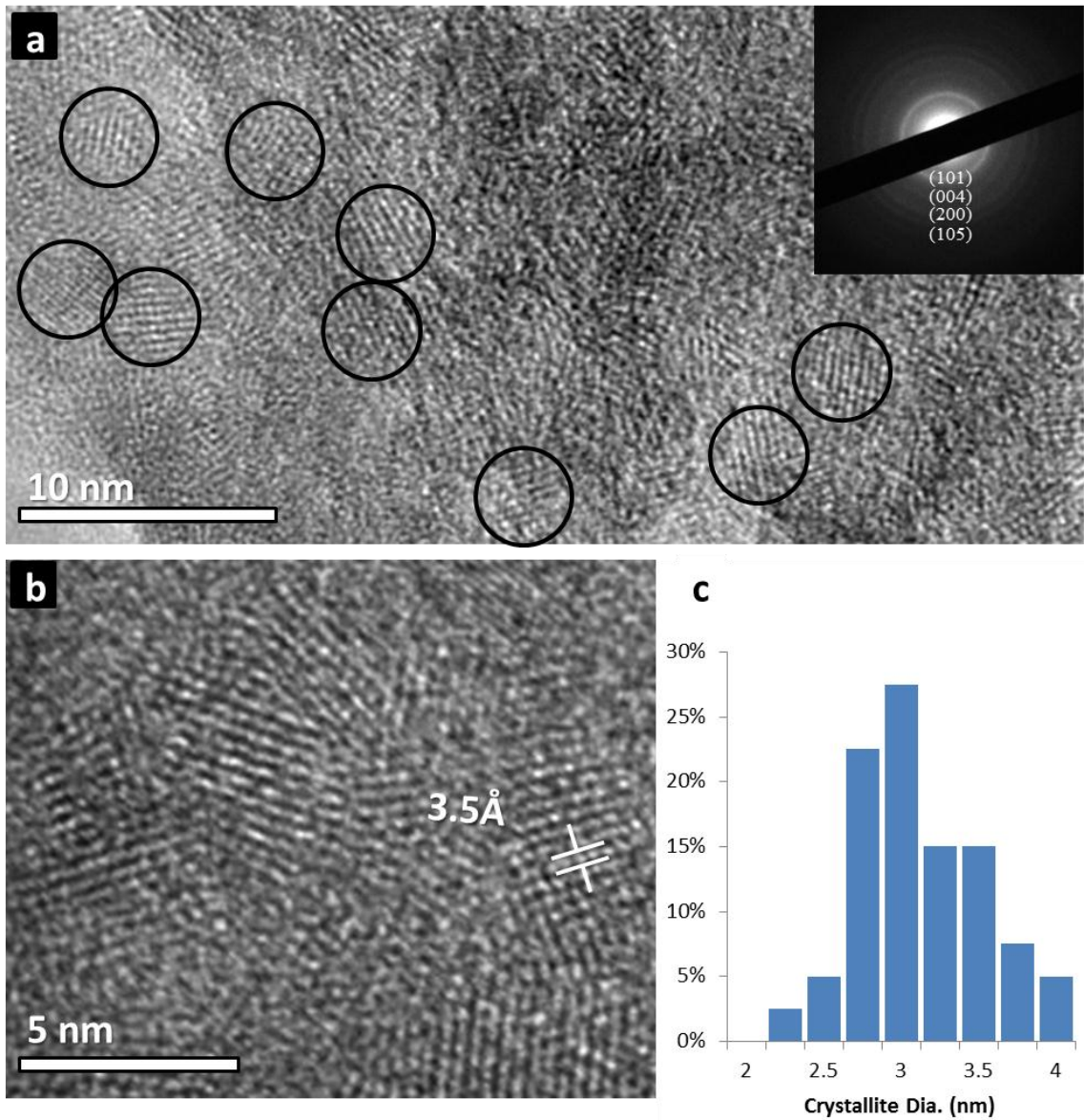


**Figure 3.17:** Bright field TEM image, with SAED inset (a), HRTEM image (b), and representative histogram (c) of TiO<sub>2</sub> synthesized at 25°C for 24 hours, the circles indicate apparent lattice fringes.

indicate the presence of nanocrystalline materials of approximately 3 nm size. The SAED insets of these images indicate the synthesized material is anatase TiO<sub>2</sub>, this is further corroborated by d-spacing measurements of  $3.52\text{\AA} \pm 0.08$  (figs. 3.16b – 3.18b). Particle sizing was performed, using TEM images prepared for each duration (i.e., 12 hr, 24 hr, and

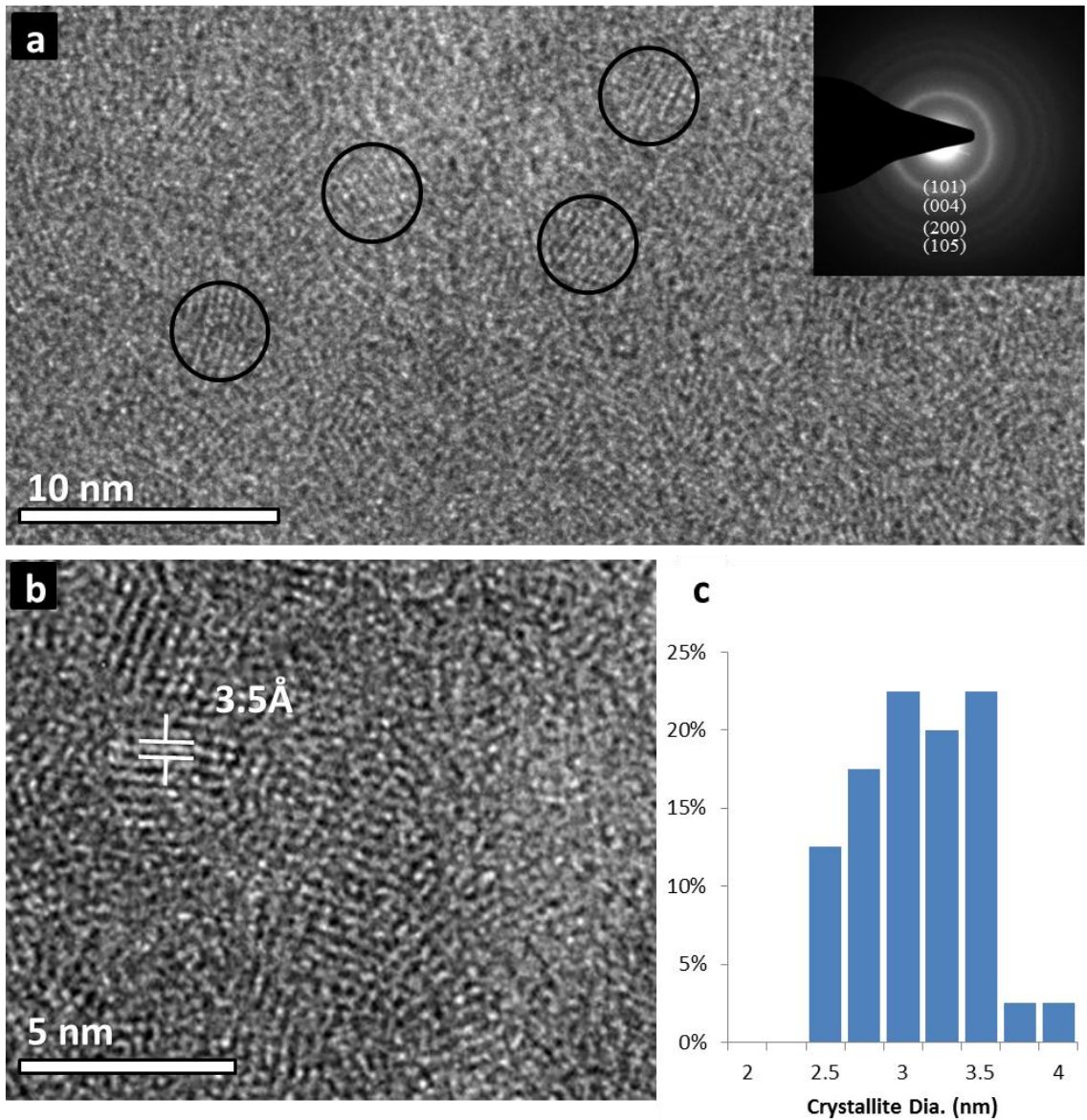


**Figure 3.18:** Bright field TEM image, with SAED inset (a), HRTEM image (b), and representative histogram (c) of TiO<sub>2</sub> synthesized at 25°C for 36 hours, the circles indicate apparent lattice fringes.

36hr), by examination of at least 40 nanocrystals per experimental set. Histograms representing the size dispersions of the as-synthesized materials (figs. 3.16c – 3.18c) show nanocrystals having size indices of  $2.72 \pm 0.37$ ,  $2.98 \pm 0.38$ , and  $2.98 \pm 0.36$ , for samples prepared for 12, 24, and 36 hours respectively.

As noted earlier, 12 hour reaction times were required in order to produce enough materials for analysis via XRD. To examine materials produced at earlier time periods, the following experimental procedure was performed. Reaction samples were prepared (0.1M TiBALDH, 0.33M urea, with initiation by injection of urease to a concentration of 0.13 $\mu$ M). The experiments were performed at room temperature

in sealed reaction vessels with magnetic stirring at 700rpm. Aliquots were removed directly from the reaction solutions at times 0, 0.25, 0.5, 1, 2, 6, 12, 24, and 48hrs. Time = 0 indicates that the aliquot was taken prior to reaction initiation by injection of urease. Sample aliquots were directly deposited onto 400 mesh holey-carbon copper grids (Ted Pella). TEM (Tecnai 12) was used to determine the approximate point in the reaction at which anatase nanoparticles became present. The pH of the solution was noted at each time point an aliquot was removed.

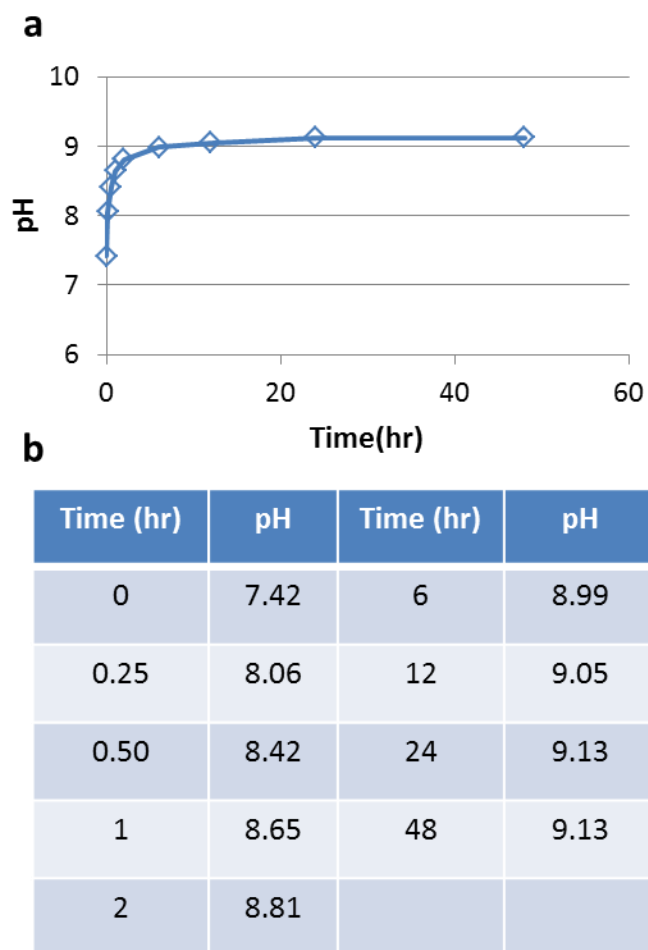


**Figure 3.19:** Plot showing the change in pH after injection of urease (a) into a TiO<sub>2</sub> synthesis solution, and (b) pH values monitored over the duration of the experiment.

The solution pH increased over the course of the experiment from the initial pH of 7.42 (prior to urease injection) to the final pH of 9.13 taken after a 48hr reaction (fig.

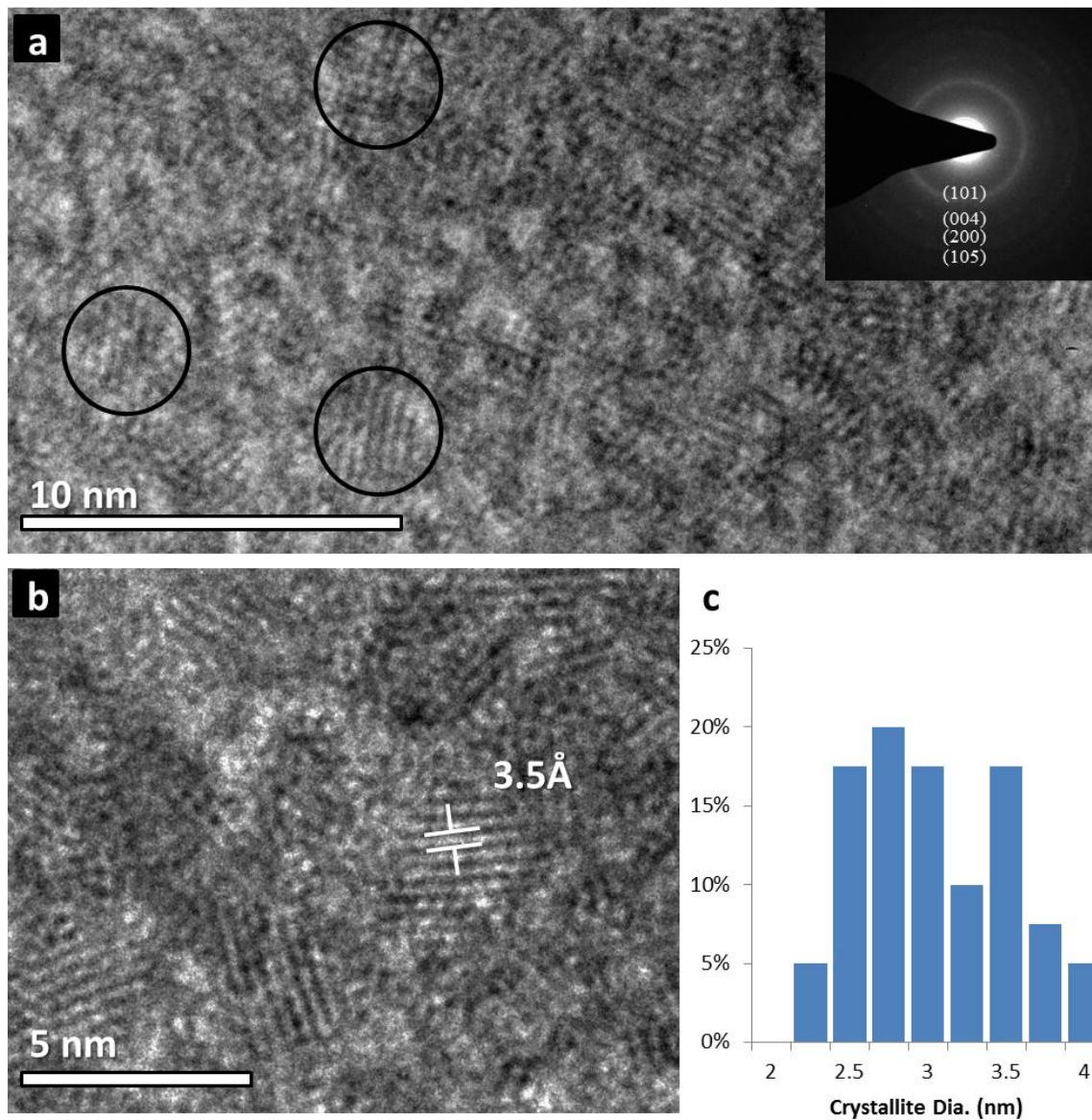


**Figure 3.20:** Bright field TEM image, with SAED inset (a), HRTEM image (b), and representative histogram (c) of TiO<sub>2</sub> synthesized at 25°C for 1 hour, the circles indicate apparent lattice fringes.

3.19a). The collected values are presented in figure 19b. TEM images, with

accompanying SAED insets, representing the samples removed at 1 and 6hrs (figs. 3.20a

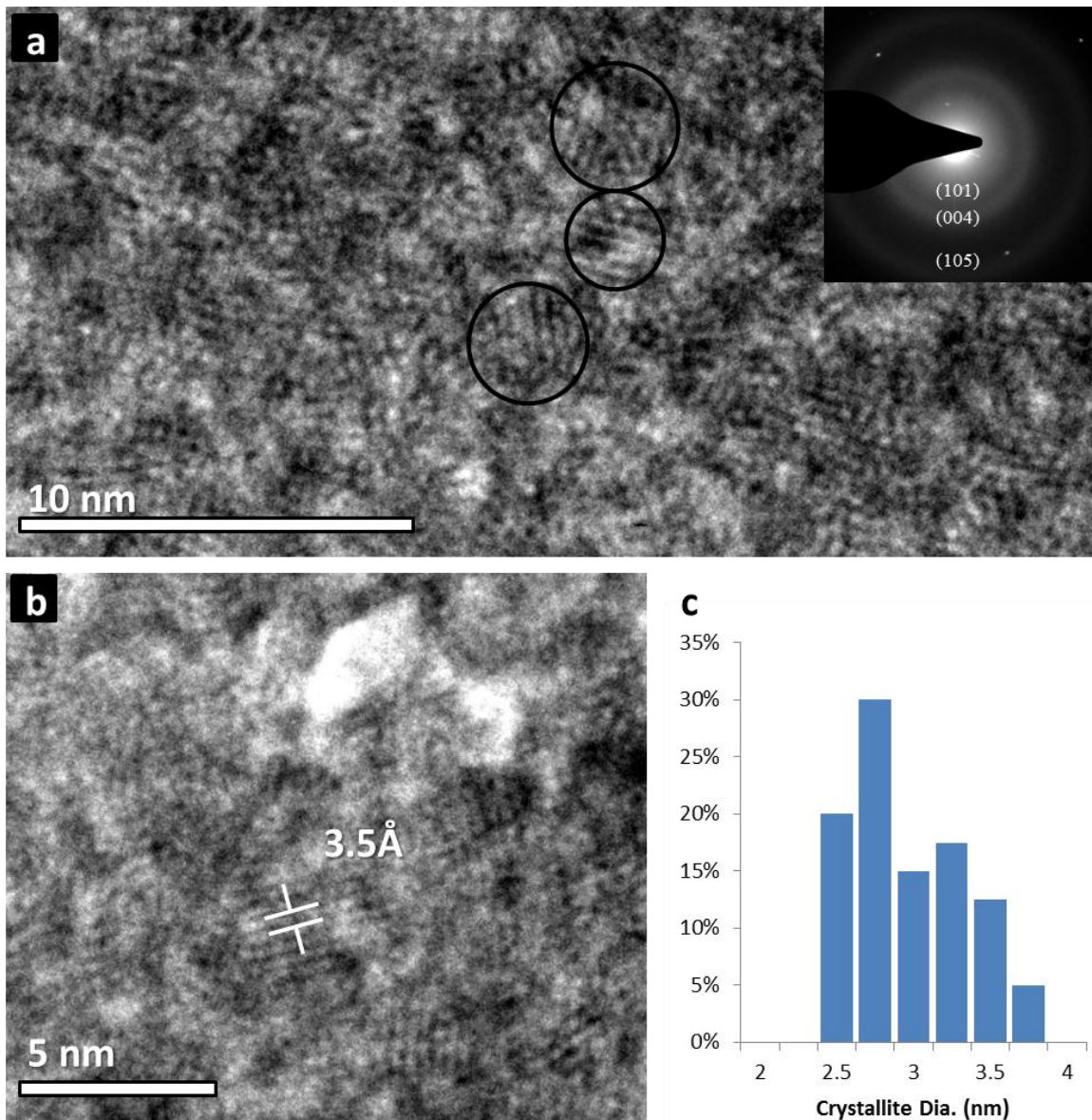


**Figure 3.21:** Bright field TEM image, with SAED inset (a), HRTEM image (b), and representative histogram (c) of TiO<sub>2</sub> synthesized at 25°C for 6 hours, the circles indicate apparent lattice fringes.

and 3.21a, respectively) show the presence of nanocrystalline anatase TiO<sub>2</sub>. Counts of 40 nanocrystals each, were performed on the associated TEM images showing size

dispersions of  $2.90\text{nm}\pm 0.41$  and  $2.84\text{nm}\pm 0.38\text{nm}$  for the 1hr and 6hr samples respectively. Crystalline  $\text{TiO}_2$  was not found in sample aliquots removed at time periods earlier than 1hr, thus it is apparent that nucleation occurs between 30 minutes (pH = 8.42) and 1 hour (pH = 8.65) into the reaction. The 6 hour time point shows anatase crystals of similar size distribution to the 12, 24, and 36hr TEM data already presented. Thus the similar size shown among the different time points suggests that any residual time spent in solution has no effect on the nanocrystal size.

### *3.2.6 Urease mediated synthesis of $\text{TiO}_2$ : precursor concentration study*

Experiments were carried out to determine the effect of variations in TiBALDH concentration. All reaction solutions consisted of 0.33M and were initiated by injection of 1mL, freshly prepared,  $3.9\mu\text{M}$  aqueous urease suspension (for a urease concentration of  $0.13\mu\text{M}$ ). Three separate TiBALDH concentrations of 0.001M, 0.01M and 0.1M were examined. The solution temperature was  $25^\circ\text{C}$  and the reaction time was 24 hours.

XRD analysis (fig. 3.22a) shows reflections for the materials produced using solutions containing 0.001M, 0.01M, and 0.1M TiBALDH concentrations. The quantity of materials synthesized decreased with a decrease in titanium precursor, thus the amount of powder used for analysis was significantly decreased in the 0.001M sample. The reflections for the 0.01M and 0.1M TiBALDH samples showed the expected peaks at  $2\theta = 25.3^\circ, 37.8^\circ, 48.1^\circ$  and  $53.9^\circ$ , indicating anatase  $\text{TiO}_2$ . However, the sample prepared using 0.001M TiBALDH showed a only a single broad peak at an approximate  $2\theta$  of 24.8. This may be attributed to the low quantity of materials, thus the average crystallite

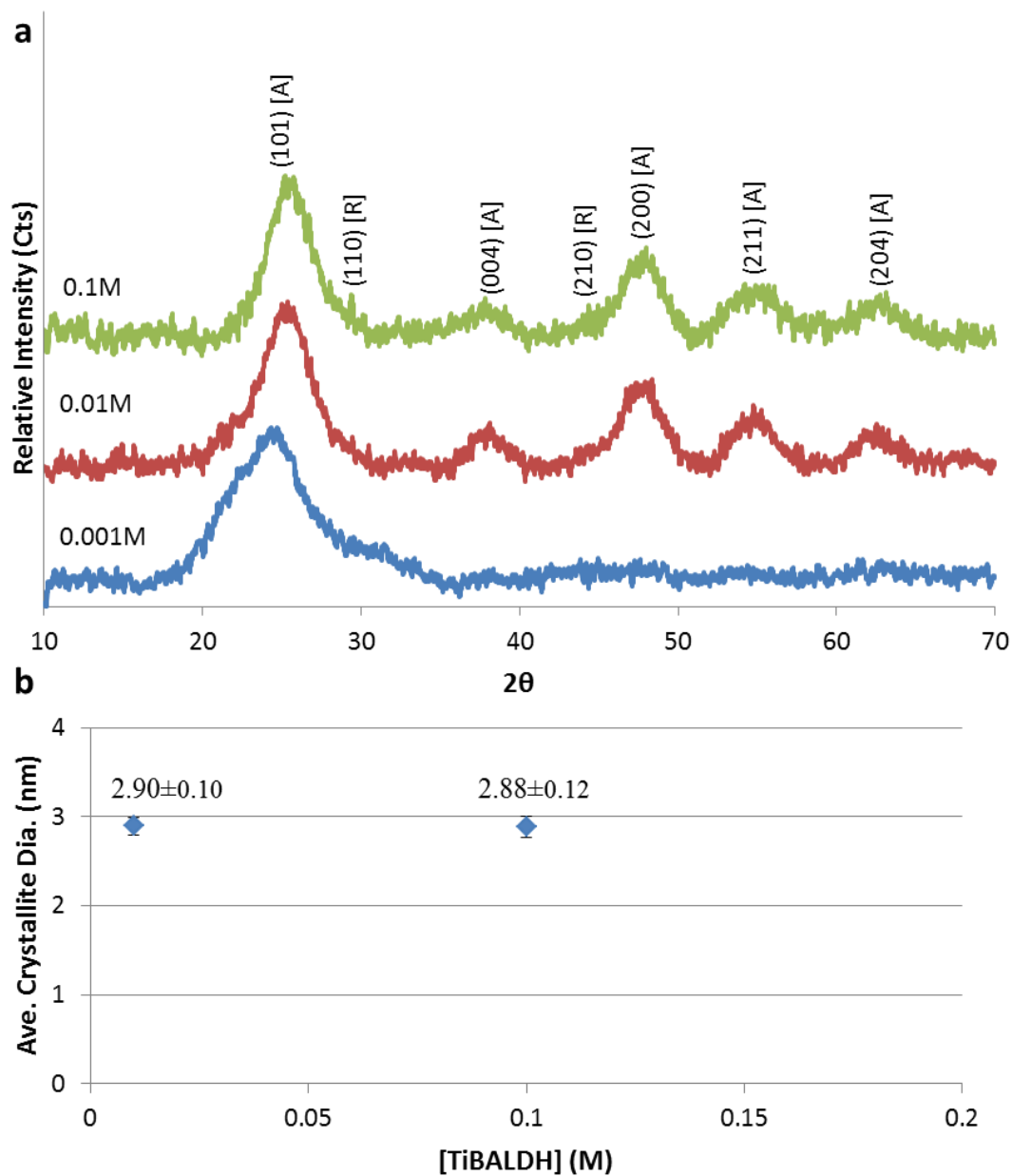


Figure 3.22: XRD patterns for materials synthesized via the urease mediated method at 25°C, with TiBALDH concentrations of 0.1M, 0.01M, and 0.001M for 24, and b) corresponding plots showing the variation in crystallite size with respect to TiBALDH concentration.

size of those samples prepared using a 0.001M concentration of TiBALDH was inconclusive. Scherer analysis performed on the (200) reflections of both the 0.01M and

0.1M TiBALDH samples showed nearly constant (within the margin of error) crystallite sizes (fig. 3.22b).

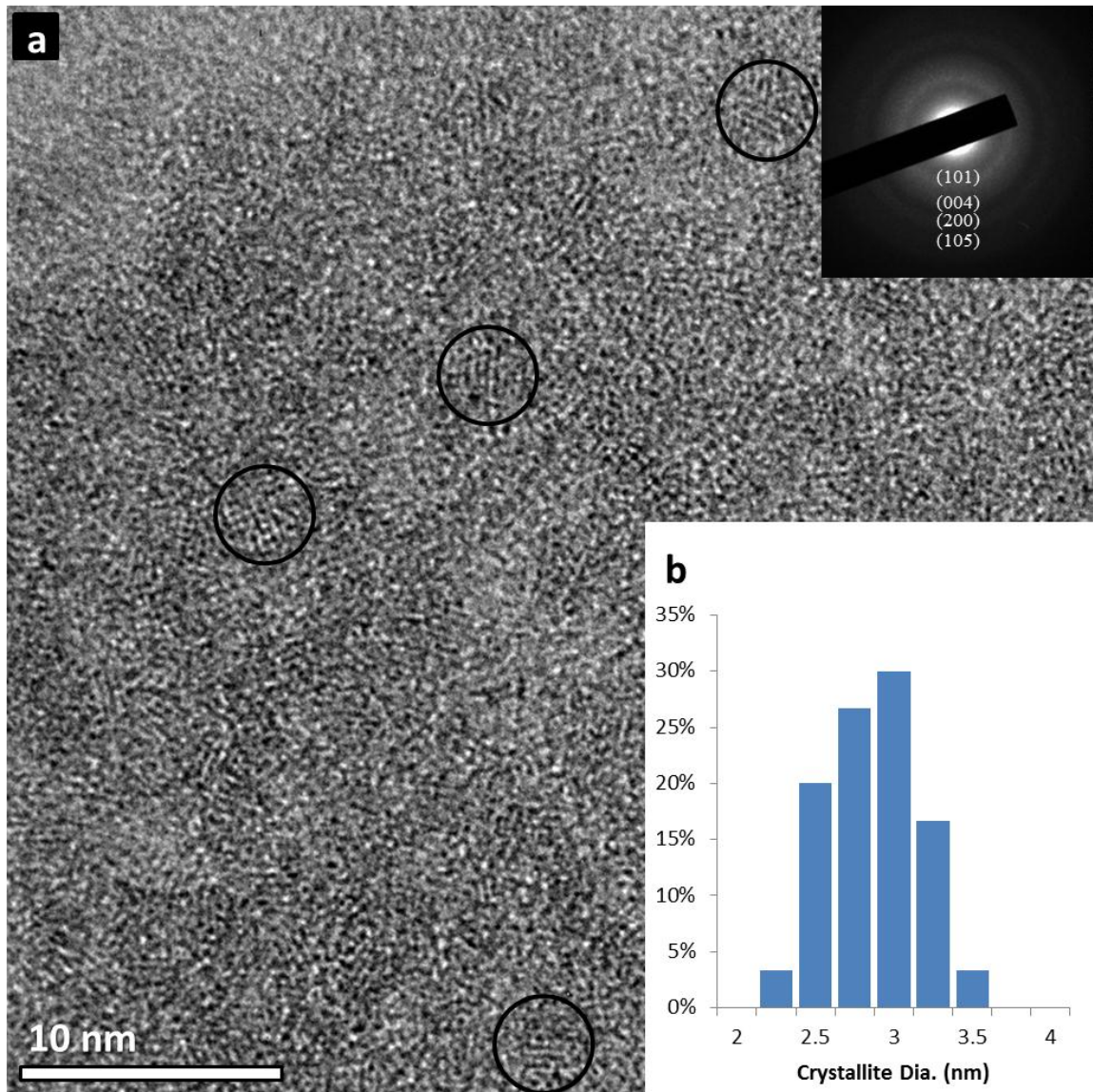


Figure 3.23: Bright field TEM image, with SAED inset (a), HRTEM image (b), and representative histogram (c) of TiO<sub>2</sub> synthesized at 25°C, with TiBALDH concentration = 0.001M for 24hours, the circles indicate apparent lattice fringes.

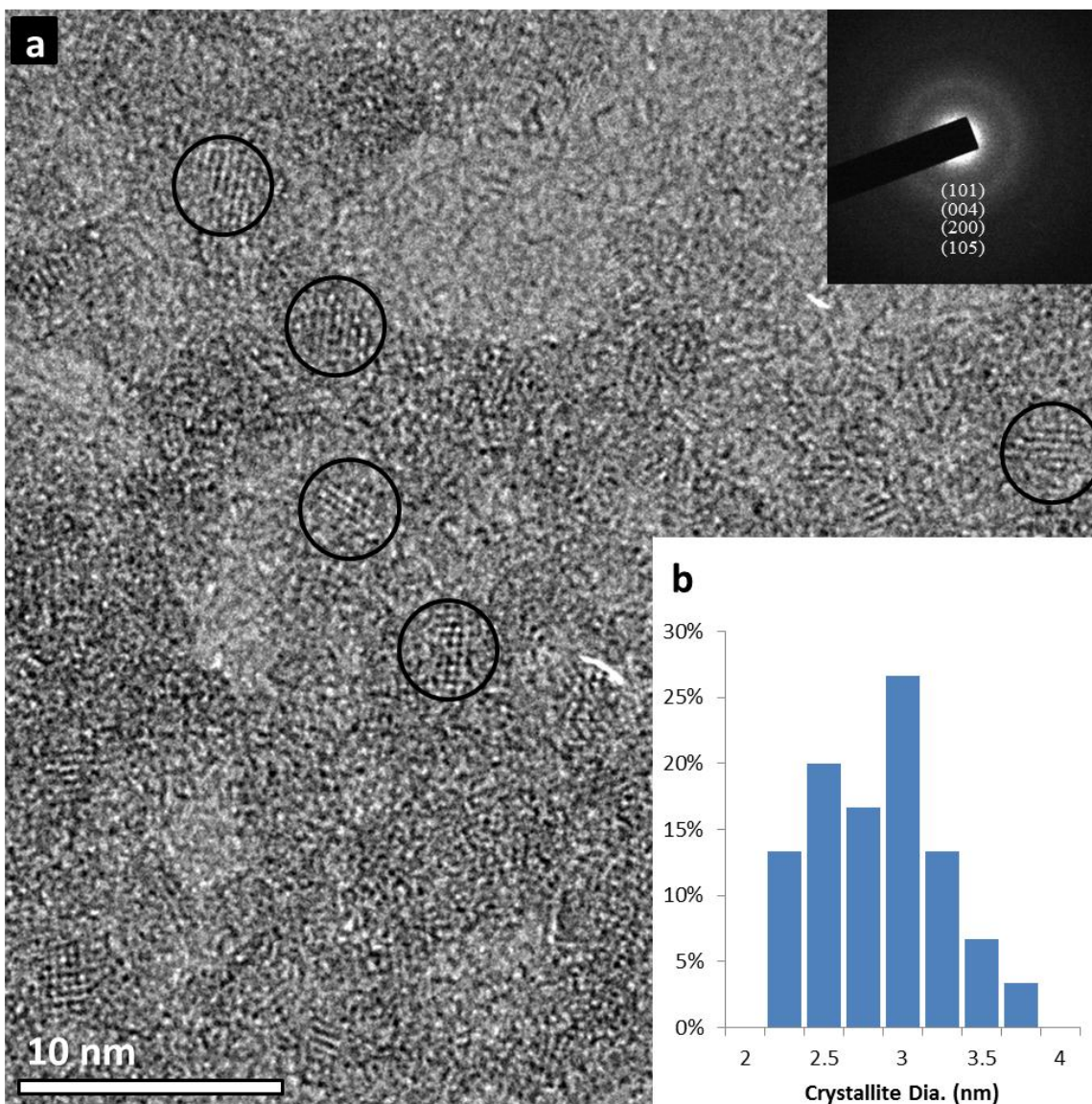


Figure 3.24: Bright field TEM image, with SAED inset (a), HRTEM image (b), and representative histogram (c) of TiO<sub>2</sub> synthesized at 25°C, with TiBALDH concentration = 0.01M for 24hours, the circles indicate apparent lattice fringes.

Due to the lack of material acquired in the 0.001M sample, the experiment was repeated using TEM analysis of aliquots directly withdrawn from the reaction solutions. The reactions were performed again following the same protocol (i.e., 0.33M urea, 0.13 μM urease, 0.001M, 0.01M, and 0.1M TiBALDH) with the exception that, instead of a

final washing and drying step, samples were directly removed from the reaction vessels after 24 hours and deposited onto 400 mesh holey-carbon copper grids (Ted Pella). The samples were then analyzed using TEM (T-120).

TEM images show nanocrystalline materials of approximately 3nm (fig. 3.23a –

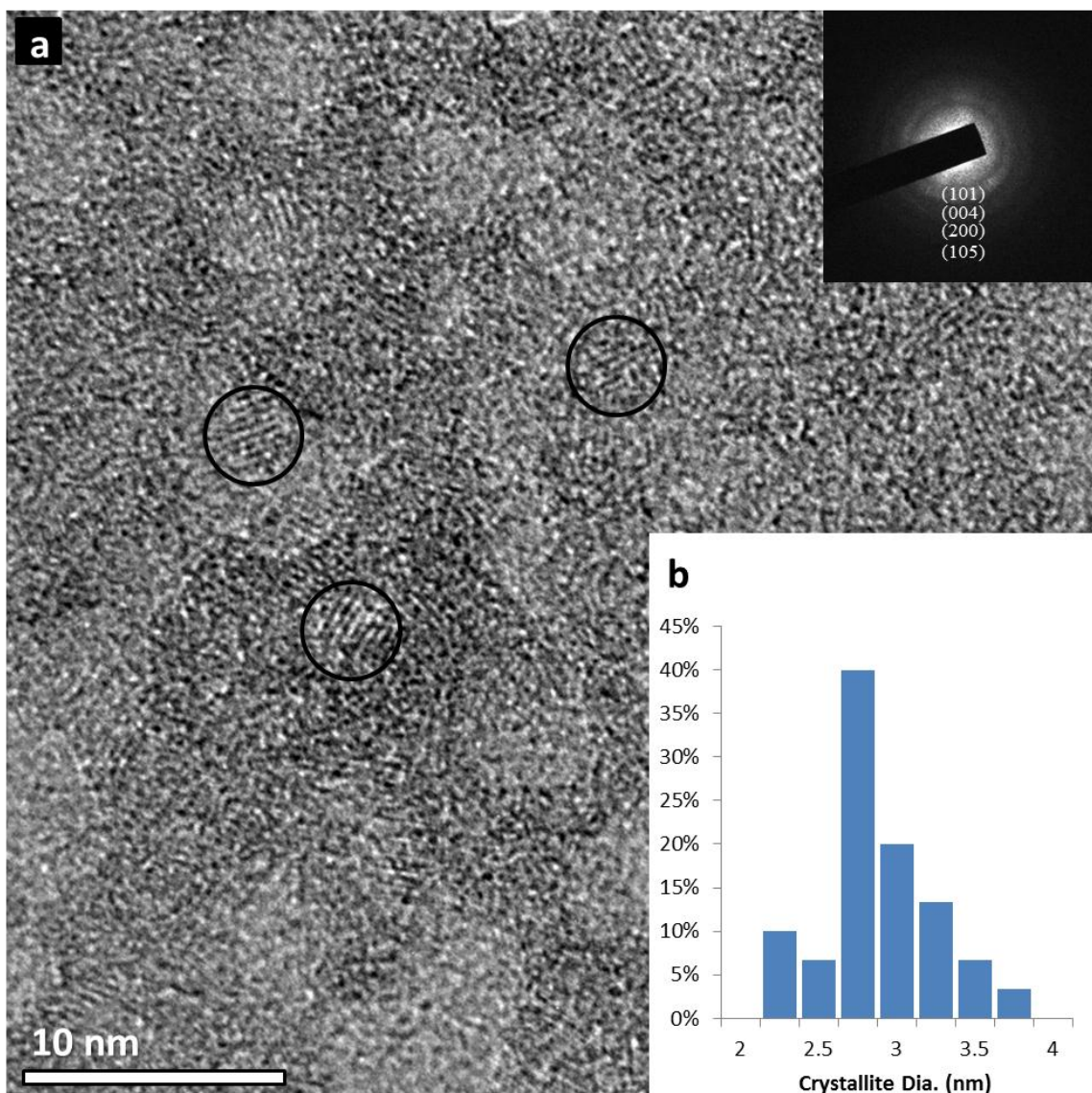


Figure 3.25: Bright field TEM image, with SAED inset (a), HRTEM image (b), and representative histogram (c) of TiO<sub>2</sub> synthesized at 25°C, with TiBALDH concentration = 0.1M for 24hours, the circles indicate apparent lattice fringes.

3.25a) for urease-mediated materials using 0.001M, 0.01M, and 0.1M TiBALDH. Inset SAED confirms the presence of nanocrystalline anatase  $\text{TiO}_2$ . Histograms (figs. 3.23a – 3.25a) were prepared by analysis of 30 distinct crystallites. The size indices were  $2.74 \pm 0.29$ ,  $2.72 \pm 0.39$ ,  $2.76 \pm 0.37$  for the 0.001M, 0.01M, and 0.1M TiBALDH samples, respectively.

The theoretical effect of precursor concentration on the critical radius of nucleating crystals is governed by eqn. 3.6. Similar to the effect of temperature, the critical radius of nucleating crystals decreases with an increase in the degree of supersaturation of the solution. This effect is stronger than the effect of temperature due to the degree of supersaturation appearing within the natural logarithm of the term. The data clearly shows that comparable crystallite sizes are achieved for each concentration of precursor. Thus, there may indeed be crystallite growth occurring but only up to a temperature limited size, as seen in previous experiments.

### *3.2.7 Room temperature synthesis of $\text{TiO}_2$ by exogenous pH adjustment*

In order to compare the monodispersity of  $\text{TiO}_2$  synthesized using the urease mediated synthesis method, versus  $\text{TiO}_2$  synthesized using exogenous pH adjustment, control samples were prepared by adding 30%  $\text{NH}_4\text{OH}$  in  $10\mu\text{L}$  increments to 25mL nanopure water until a pH of 9.14 was achieved (pH 9.14 was the maximum pH achieved in urease mediated synthesis solutions after 36 hour room temperature incubation). TiBALDH was added to the control samples (0.1M) and additional nanopure water to a reaction volume of 30mL. The control samples were then incubated at  $25^\circ\text{C}$  for 36 hours.

The prepared materials were then washed and dried in the manner detailed at the beginning of the experimental section.

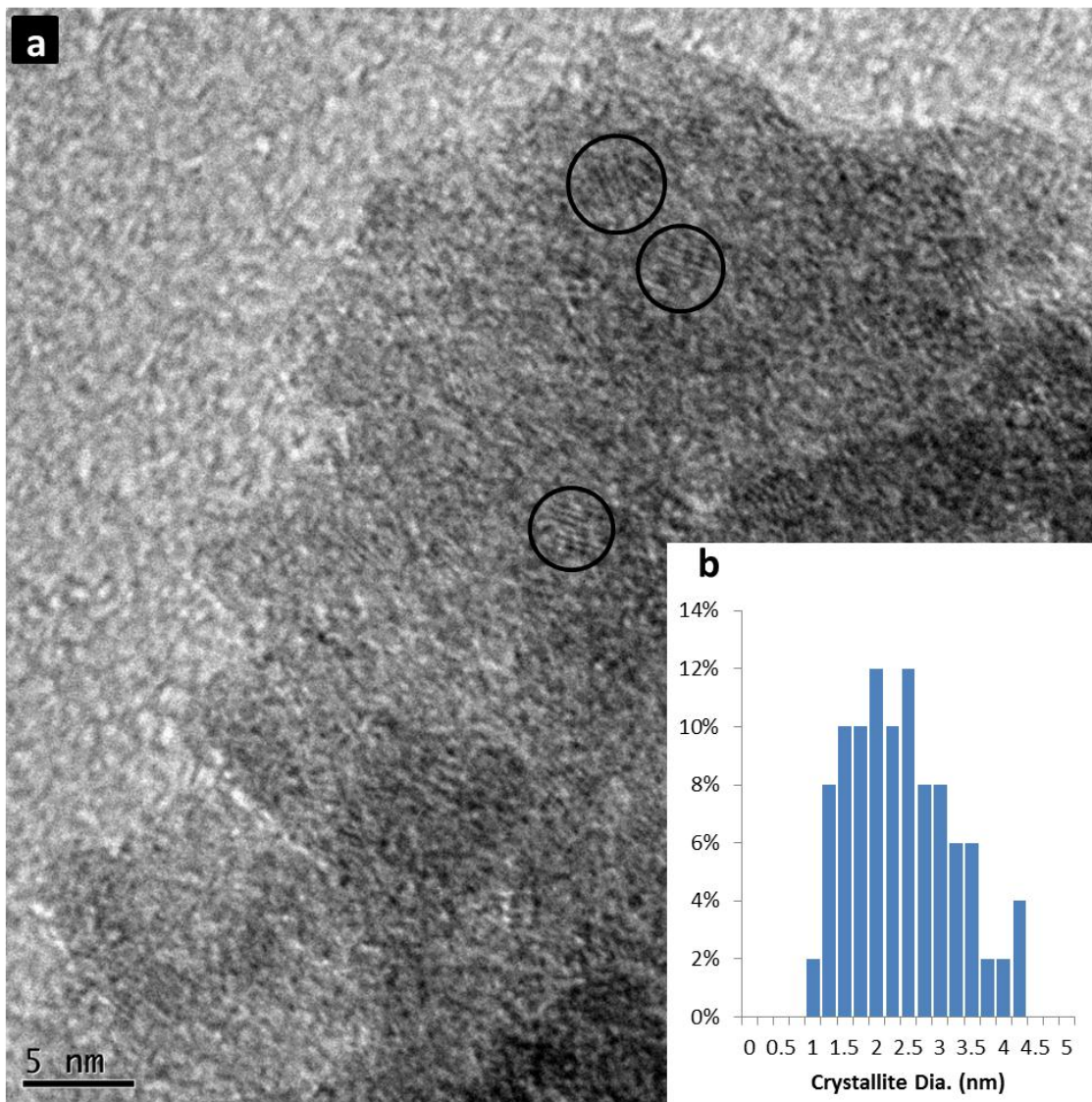


**Figure 3.26: Bright field TEM image (a), and representative histogram (b) of TiO<sub>2</sub> synthesized at 25°C, in pH 9.14 solution exogenously prepared using NH<sub>4</sub>OH.**

Analysis of the TEM images for the sample prepared through exogenous pH adjustment (fig. 3.26a) show the prepared nanocrystals to be slightly smaller than those

prepared via urease synthesis but with a size distribution ( $2.28\text{nm}\pm 0.80$ ) nearly double that of the urease mediated method.

### *3.3 Discussion/Conclusion*

Initial experiments were used to determine the Michaelis-Menten parameters of the enzyme in the synthesis solutions. Generally, Michaelis-Menten experiments are carried out under controlled pH, however, variation of solution pH expected and essential to this system, thus pH was not restricted by the addition of buffer reagents. The values presented show that there is an increase in both the  $K_M$  and the  $V_{max}$  of the reaction solutions corresponding to an increase in solution temperature. This trend is expected in enzymatic catalysis due to the Arrhenius-type rate dependence (fig. 3.44a and b) of these reactions at temperatures below the specific enzymes thermal denaturation temperature. Urease is known to thermally denature at or near temperatures of  $80^\circ\text{C}$  and thus, experiments in this thesis focused on temperatures below this point. For the urease mediated synthesis solutions the maximum rate of reaction was lowest at room temperature. This is beneficial for the synthesis of  $\text{TiO}_2$  in that it allows time for the titanium precursor to homogeneously distribute throughout the reaction solution prior to the production of hydroxyl ions and subsequent hydrolysis of the titanium precursor.

Synthesis reactions were carried out under various conditions (e.g., temperature, time, and precursor concentration) and predominantly showed synthesis of anatase nanocrystals. It is anticipated that a metastable phase such as anatase would form due to the fact that the energy landscape the reaction sees, being at low temperature, is often one

that passes through metastable phases on its way to the final crystalline state (i.e., rutile). These pathways often have lower energy barriers, as is such for nucleation of anatase vs. rutile<sup>118</sup>. In fact, many methods to TiO<sub>2</sub> often form anatase first<sup>119,120</sup>. Structurally, the long-range arrangement of the TiO<sub>6</sub> octahedra in anatase is less-constrained than rutile<sup>121</sup>. In addition, anatase has a lower surface free energy, even though rutile has a lower Gibbs free energy<sup>122,123</sup>, and thus, anatase may be the more favored crystalline phase due to the high surface energy of rutile crystallites<sup>118</sup>.

**Table 1: Collected crystallite size distributions.**

Experimental Set	Sample Parameter	Particle Size (nm)	Experimental Set	Sample Parameter	Particle Size (nm)
Temperature Study	25°C	2.85±0.33nm	Time Study	1hr	2.90±0.41nm
	40°C	3.03±0.31nm		6hr	2.84±0.38nm
	60°C	2.04±0.39nm		12hr	2.72±0.37nm
[TiBALDH]	0.001M	2.74±0.29nm		24hr	2.98±0.38nm
	0.01M	2.72±0.39nm		36hr	2.98±0.36nm
	0.1M	2.76±0.37nm			

Size and size distributions of each specimen were determined by measuring at least 40 (figs. 3.7a-3.9a, 3.16a-3.18a, 3.20a, 3.21a, and 3.26a) or in some cases 30 (figs. 3.23a-3.25a), nanocrystals per sample (from TEM micrographs). Representative histograms are designated (b) in the above noted images. It is clear that the samples demonstrate a narrow size distribution as shown in table 1, which indicates a coordinated hydrolysis and condensation of the precursor leading to controlled nucleation and growth of TiO<sub>2</sub> nanocrystals. In comparison, anataseTiO<sub>2</sub> prepared without enzyme (i.e., by adding exogenous base) at 25°C, similar pH, and reaction time of 36 hours (fig. 3.26b)

show smaller average crystallite domains (2.28 nm +/- 0.80), but with a larger distribution, highlighting the uniformity of the enzyme-mediated process. These coordinated reactions are related to the hydrolytic stability of TiBALDH due to the interaction of adjacent oxygen and carboxylic functional groups with the metal center. This conjugate system allows for delocalization of electrons away from the oxygen molecule complexed to the central metal ion, resulting in a reduction of the Lewis basicity of the coordinated oxygen atom<sup>105</sup>. Thus, the homogenous dispersion of urease throughout the solution coincides with a homogenous increase in concentration of hydroxide ions (OH<sup>-</sup>), which enables a simultaneous, nucleophilic attack of free hydroxide ions on the juxtaposed bidentate ligands coordinatively attached to a central Ti<sup>4+</sup> ion<sup>107</sup>. These nucleophilic ions hydrolyze the TiBALDH, leading to the formation of fully (and partially) hydrolyzed species that can participate in condensation reactions. This is advantageous over adding an exogenous base that will react with TiBALDH molecules located at the surface of the reaction media before those that are at the bottom of the reactor.

The initial pH of the synthesis solutions is approximately 7.8, thus the increase over a 1 hour period, from the initial pH to the synthesis pH of approximately 8.65, represents a near order of magnitude increase in hydroxide ions. This uniform generation of hydroxide ions in the reaction solution ensures a significant fraction of the TiBALDH molecules will hydrolyze at the same rate. If the speciation of  $\text{Ti}(\text{BALDH})_{2-n}(\text{OH})_{2+n}$  is nearly the same, then, the rate of growth of condensed species will also be similar and

thus, the induction time to nucleation (i.e., the time from the solution acquiring a state of supersaturation to the formation of nuclei of critical size<sup>124</sup>) will be uniform. The induction time is related to the nucleation rate given by<sup>125</sup>:

$$J_n = A \exp(-\Delta G_n / k_B T) \quad (3.7)$$

where,  $A$  is a constant,  $\Delta G_n$  is the Gibbs free energy change required for nucleation,  $k_B$  is the Boltzman constant and  $T$  is the temperature. This expression can further be expressed by:

$$J_n = A \exp(-B\alpha^3 / \sigma^2) \quad (3.8)$$

where,  $B$  is a constant,  $\alpha$  is the interfacial energy and  $\sigma$  is the supersaturation. This equation shows that the nucleation rate is strongly dependent on the supersaturation. Thus by controlling the concentration of (i) enzyme, (ii) urea, (iii) TiBALDH, we can control the hydrolysis of TiBALDH to form Ti-OH species, which subsequently condense to form Ti-O-Ti clusters, and thus by controlling the supersaturation the nucleation rate is uniform throughout the solution.

The crystallite diameters of the synthesized TiO<sub>2</sub> were approximately constant regardless of reaction duration, solution temperature, or precursor concentration and thus, significant growth was hindered. It has been shown that lactic acid has an affinity for TiO<sub>2</sub> surfaces<sup>126</sup> and thus the hydrolyzed lactato ligand by-products likely adsorb to the surface of the newly formed nanocrystals, hindering diffusion of growth units onto the crystallite surface. Mockel *et al.* demonstrated this phenomenon<sup>105</sup> by injecting

ammonium lactate into a hydrothermal reactor at the onset of a reaction using TiBALDH as a precursor to form TiO<sub>2</sub>. The result was a 50% size reduction of TiO<sub>2</sub> crystallites versus those prepared without extraneous lactate groups. The reactions in this study are at significantly lower temperatures than hydrothermal conditions, and thus it is also feasible that growth can be limited, not only due to lactate absorption but also from sluggish growth kinetics.

UV-Visible spectra (Figure 3.10) were also obtained for TiO<sub>2</sub> synthesized at 25°C, 40°C, and 60°C for 36 hours. The band gap measurements from this data were determined to be 3.22eV, 3.21eV, and 3.19eV for samples prepared for 36 hours at 25°C, 40°C, and 60°C, respectively. Although there is a slight decrease in the observed band gap with increasing synthesis temperature, the results are within the margin of error and are therefore considered constant. The measured band gaps are also similar to those observed in previous investigations and reflect the predicted band gap for anatase TiO<sub>2</sub>.

This chapter demonstrates a bio-mediated approach, using the hydrolytic enzyme urease, to induce a uniform dispersion of anatase TiO<sub>2</sub> at room temperature. This is achieved through coordination of enzyme with urea in a solution containing a hydrolytically stable TiO<sub>2</sub> precursor. The lag time between injection of urease and generation of hydroxide ions in solution affords a coordinated hydrolysis and condensation of precursor molecules, resulting in a single-burst nucleation event. In addition, the use of an enzyme to generate reagents (i.e., hydroxide ions) circumvents the need to thermally decompose formamide or urea, and thus, the reaction can be sustained

at room temperature, which enables the growth of these materials on polymeric substrates (e.g., electrically conductive polymers as electrodes for flexible sensitized solar cells).

## Chapter 4: Immobilized Urease Mediated Synthesis of TiO<sub>2</sub>

### 4.1 Enzyme Immobilization

Although there are a variety of uses for enzymes, there are a number of limitations that can be overcome through immobilization. The benefits of using enzymes immobilized onto a substrate are twofold: (i) ease of separation of the enzyme from the catalyzed product, and (ii) the ability to reuse the substrate for subsequent reactions<sup>128</sup>. Some researchers have also reported increases in stability with respect to pH and temperature conditions compared with the normal operating conditions of the enzyme<sup>129</sup>. It is speculated that this increase in stability may be due to the three-dimensional stabilization induced from a closely packed field of enzymes. There have also been published reports of increasing activity of immobilized enzymes versus native (free-floating) enzymes<sup>130</sup> in solution, however, other researchers have shown substantial decreases in the relative activity of immobilized enzymes<sup>131</sup> versus that of the native enzyme in solution.

There are three primary methods of enzyme immobilization: support binding, entrapment, and chemical cross-linking. Immobilization of enzymes onto a carrier support relies on physisorption of the enzyme to a solid carrier. The carriers used in support binding may be inorganic (e.g., glass<sup>132</sup>, alumina<sup>133</sup>, silica<sup>134</sup>, etc.) or organic (e.g., structural proteins such as collagen<sup>135</sup>, globular proteins such as albumin<sup>136</sup>, or carbohydrates<sup>137</sup>). Support binding methods are advantageous in that activation can be typically achieved without secondary reagents and with minimal activation steps<sup>138</sup>.

However, physical adsorption provides relatively weak binding of the enzyme to the carrier support, which can prove unstable under industrial reaction conditions<sup>139</sup>. Entrapment methods encapsulate the enzymes in porous networks of an insoluble matrix material such as silica sol-gels<sup>140</sup>, or more recently, in bio-mimetically synthesized silica<sup>141</sup>. Entrapment methods are attractive because they are cheap, relatively simple methods, and may be prepared under fairly mild conditions, nevertheless the entrapment matrix can induce mass transfer/diffusion limitations which may lower the overall activity of the contained enzymes<sup>142</sup>. Chemical cross-linking covalently bonds an enzyme to a carrier substrate and thus establishes a more robust catalytic surface without the transport limitations intrinsic to entrapment methods.

Due to the reaction conditions characteristic of the urease mediated synthesis of TiO<sub>2</sub> (e.g., pH ~ 9.2, stirring of the reaction solution, removal and reuse of the immobilized substrate) the bond strength inherent in covalent binding through chemical cross-linking was deemed optimal for this study. Thus, in order to test the reusability of the enzyme as an effective catalyst for nanomaterial synthesis, an immobilization strategy was developed that utilized alkane thiol linkers bound to a gold substrate. Based on the high affinity of organosulfur compounds for gold<sup>143,144</sup>, self-assembled monolayers (SAMs) may be formed by the immersion of a clean gold substrate into a solution of  $\omega$ -terminated alkanethiols<sup>145,146</sup>. The monolayers are well ordered with densely packed terminal groups<sup>147</sup>. The SAM layers described herein are ordered assemblies consisting of

a thiol head group, a ten carbon chain spacer group, and a carboxylic acid terminal functional group.

The conjugation of the urease enzyme to the carboxy terminated alkanethiol SAM layer has been summarized in the reaction scheme shown in figure 4.1. First, gold (111)

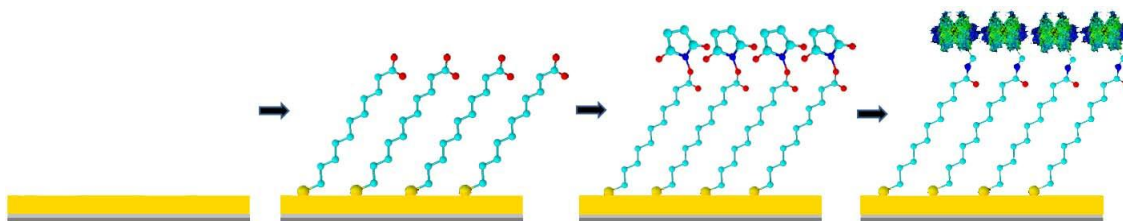


**Figure 4.1: Urease immobilization scheme. Gold (111) is overlaid on a titanium coated 4” silicon substrate, followed by SAM functionalization. Urease conjugation is achieved using EDC/NHS coupling chemistry.**

overlaid on a titanium coated 4” silicon substrate is functionalized by incubation of the gold substrate in an ethanolic solution of 11-mercaptoundecanoic acid (MUA). This procedure is followed by the amidation of the functionalized gold substrate using EDC/NHS coupling chemistry. EDC/NHS coupling proceeds through the formation of *O*-acylurea via the addition of the OH group of the carboxylic acid across one of the carbodiimide double bonds<sup>148</sup>. It has been demonstrated that the more stable *n*-acylurea may form quickly in aqueous solution<sup>149</sup> and thus simultaneous reaction with NHS may be employed to competitively form a more stable intermediate for amide coupling<sup>150</sup>. Nucleophilic attachment by the NHS molecule will result in the release of an EDC urea derivative and the formation of the succinimidyl ester (-COOSuc) functionalized alkane thiol. Amide coupling to the enzyme to the SAM functionalized gold substrate now proceeds via a primary amine present in a surface bound lysine residue<sup>151</sup>. Urease

immobilized in this manner has been researched extensively for use in detection of urea in bodily fluids as an indicator of abnormal kidney functioning<sup>152,153,154</sup> as well as a method for identification of urea-contaminated agricultural waste waters<sup>155</sup>.

#### *4.2 Experimental/Discussion*

**Immobilization of Urease:** A 5nm layer of Titanium was first evaporated, via E-beam evaporation (Temescal BJD 1800), onto a 4" silicon (100) wafer (Ted Pella) followed by evaporation of a 50nm gold layer. The wafer was then cut into 3cm<sup>2</sup> pieces which were subsequently washed in "piranha solution" (3:1 H<sub>2</sub>SO<sub>4</sub>/H<sub>2</sub>O<sub>2</sub>) for 1 hour and rinsed in nanopure H<sub>2</sub>O. The 3cm<sup>2</sup> gold pieces were then rinsed in 100% ethanol and immersed in separate 10mM ethanolic solution of MUA, purchased from Sigma-Aldrich. The 3cm<sup>2</sup> gold pieces were allowed to incubate for 24 hours at room temperature to enable self-assembly. After 24 hours, the self-assembled monolayer (SAM) of MUA coated gold substrates were rinsed in 100% ethanol and dried under argon gas. In order to couple the enzyme to the wafer, the SAM layer was activated via EDC/NHS coupling chemistry as follows: a 5mM aqueous solution of 1-ethyl-3-[3-dimethylaminopropyl] carbodiimide hydrochloride (EDC) and N-hydroxysuccinimide (NHS), both chemicals purchased from Sigma Aldrich, was prepared and incubated under argon flow for 15 minutes. After 15 minutes the SAM functionalized gold wafers were added to the solution and incubated for an additional 90 minutes under argon flow. Following the EDC/NHS activation, the wafers were then rinsed in nanopure water and dried under argon. 2mL of a 4.0μM urease suspension (pH 7.3) in sodium phosphate buffer (PBS) was placed directly on top of the

EDC/NHS activated wafers and stored for 24hrs at 4°C. Following enzyme immobilization, the wafers were washed with and stored in PBS buffer at 4°C.

#### 4.2.1 Verification of urease immobilization

As a consequence of enzymatic decomposition of urea (and subsequent introduction of ammonia into the reaction solution), there will be a corresponding increase in the solution pH, thus, a simple method of verification for the presence of immobilized urease is to monitor the change in pH over time on introduction of urea. A urease

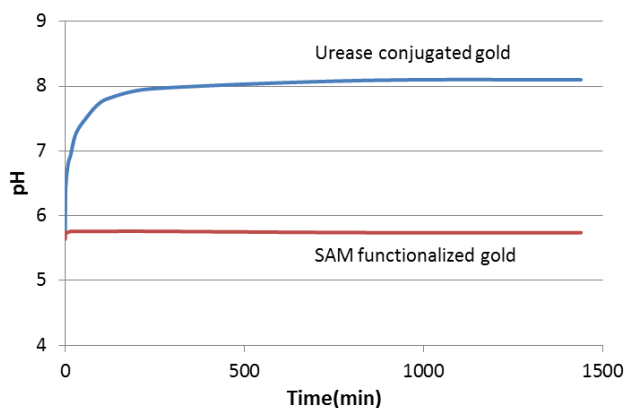


**Figure 4.2:** Plot showing the change in pH with respect to time for urease conjugated and SAM functionalized, gold wafers after injection of urea to the reaction solution.

conjugated, SAM functionalized gold wafer was inserted, gold side down, into a small Teflon holder and then placed in a beaker containing 18.5mL of 1.35M aqueous urea solution, a pH probe was immediately immersed into the reaction solution. The solution pH was continuously monitored over a 24hr period. At the same time, SAM functionalized gold wafers, that had not proceeded through the urease conjugation step, were inserted into control solutions (18.5mL, 1.35M urea). The pH of the control solution was also monitored for the same 24hr period. The gold wafer with SAM deposition maintains a nearly constant pH of 5.76 throughout the duration of the experiment. The urease conjugated wafers show an immediate increase in pH which continues to increase

linearly until a pH of approximately 7.30 is reached. At this point the rate of pH increase begins to slow as the bulk of the substrate urea has now been decomposed. The pH continues to increase until a final pH of 8.1 is reached, approximately 14hrs into the reaction, and remains constant over the duration of the experiment. The cessation of pH increase is due to the complete decomposition of the urea substrate and thus, there is no subsequent production of ammonia and corresponding release of hydroxyl ions into solution.

For further verification of immobilization and quantitation of enzyme packing density, immobilized samples were interrogated with a Veeco dimension 5000 Atomic Force Microscope (AFM) in tapping mode. The urease-immobilized gold substrates were adhered to an AFM puck using carbon tape and imaged using silicon cantilevers at a frequency of 300 kHz and spring constant of 60 N/m.

Images 4.3a and 4.3d represent the as-prepared gold surface where figure 4.3a has a scan area of 2.5 $\mu$ m and figure 4.3d has a scan size of 500nm. Based on AFM analysis, the evaporated gold layer consisted of particles between 30nm to 182nm in diameter and a relatively smooth surface topography. Figures 4.3b, e, and g represent AFM images of SAM functionalized gold substrates at scan areas of 2.5 $\mu$ m, 500nm, and 250nm, respectively. AFM images of the observed surface structures of these SAM-functionalized layers followed the same topography displayed by the gold layers but with an obvious roughening at the nanoscale indicating SAM coverage. Figures 4.3c, f, and h represent AFM images of urease enzyme that is covalently bound to the SAM surface.

The size of the cantilever would not allow high enough resolution to differentiate

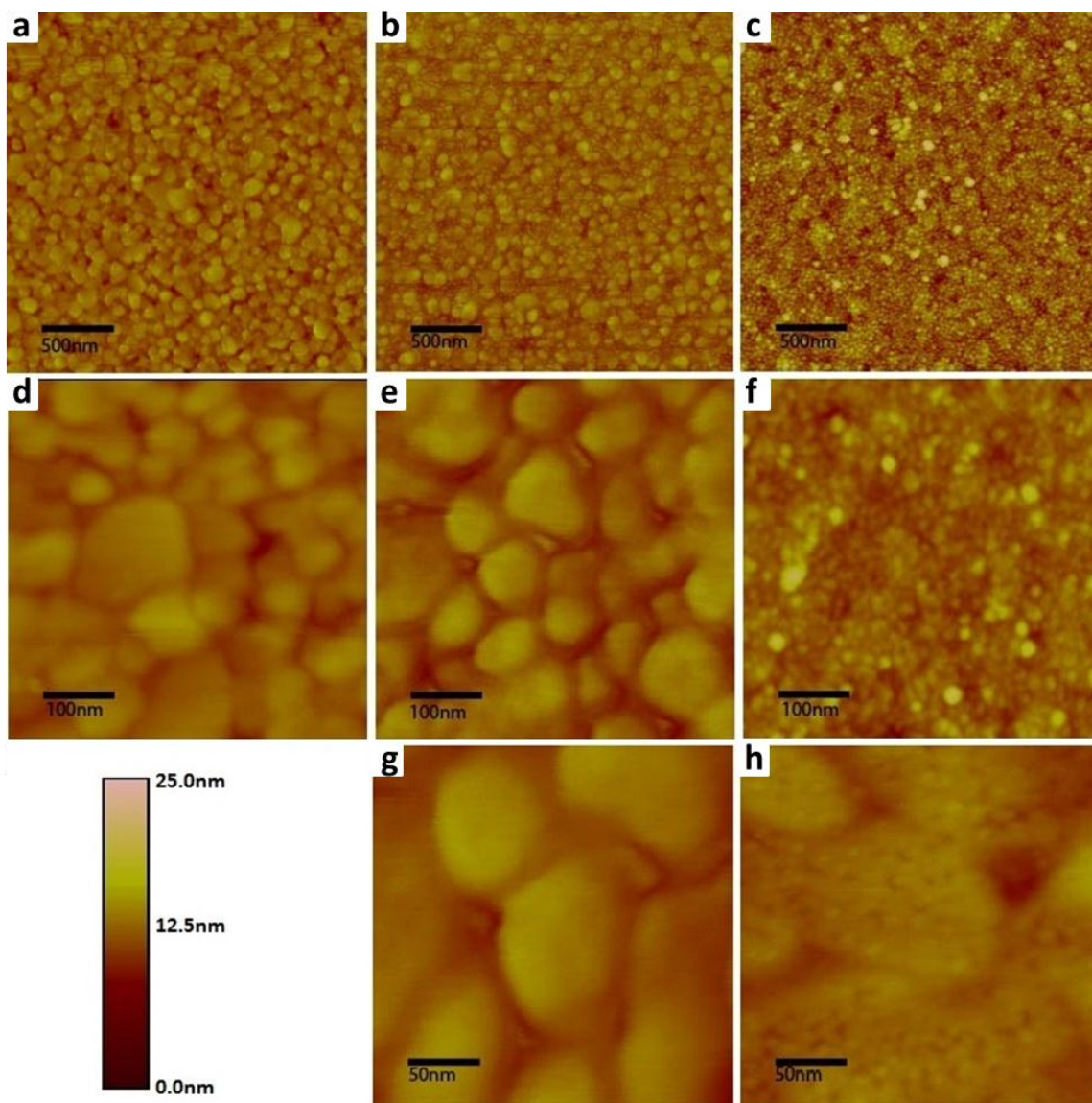


**Figure 4.3:** AFM images for a)  $2.5\mu\text{m}^2$  area of gold substrate, b)  $2.5\mu\text{m}^2$  area of SAM functionalized gold substrate, c)  $2.5\mu\text{m}^2$  area of urease immobilized onto SAM functionalized gold substrate, d)  $500\text{nm}^2$  area of gold substrate, e)  $500\text{nm}^2$  area of SAM functionalized gold substrate, f)  $500\text{nm}^2$  area of urease immobilized onto SAM functionalized gold substrate, g)  $250\text{nm}^2$  area of SAM functionalized gold substrate, and h)  $250\text{nm}^2$  scan of urease immobilized onto SAM functionalized gold substrate.

between the gold surface and SAM surface ( $\sim 1.2$  nm height differential), but a distribution of smaller particles can be seen in all three image sets for the enzyme

immobilized substrates, indicating the presence of urease on the surface. The packing density of the immobilized urease was determined by manually counting the visible structures on all AFM images with  $500\text{nm}^2$  scan areas (fig. 4.3f). The determined packing density is  $0.14 \text{ urease/nm}^2$  correlating to  $4.2 \times 10^{13} \text{ urease/3cm}^2$  wafer. Figure 4.3h appears to show that the enzyme is uniformly distributed across the substrate. In addition, height differentiation between the SAM layer and of enzyme was on the order of 12nm indicating that a single monolayer of enzyme was deposited (fig. 4.3g). The urease layer shown in figure 4.3f also appeared to be construed of objects with an average diameter of approximately 12.67nm. Previous reports indicate that urease is composed of 6 sub-units with a diameter of  $60.8\text{\AA}$  (based on a spherical sub-unit)<sup>156</sup>. This implies that for the 6 sub-unit hexamer the lateral diameter is approximately

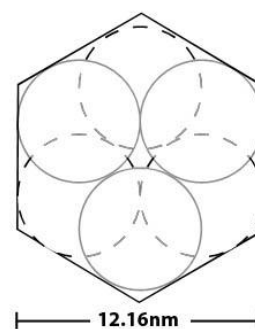


**Figure 4.4: Schematic diagram of the hexameric urease enzyme containing 6 equal subunits.**

12nm (fig 4.4). This corresponds well to the structures revealed by AFM on the urease-immobilized substrate. Based on the measured increase in solution pH after injection of urea as well as AFM images showing the urease enzyme conjugated onto a SAM functionalized gold surface, the aforementioned immobilization procedure was deemed successful.

#### *4.2.2 Reusability of urease conjugated gold substrate*

The reusability of the urease-immobilized substrates was determined by cyclic testing of pH as a function of time. The immobilized substrates were immersed in a

20mL, 1.0M aqueous solution of urea at room temperature. The pH of this solution was concurrently monitored. After the first cycle, the wafer was removed from solution, washed in pH 7.3 PBS and stored overnight in PBS at 4°C. 4 subsequent cycles were performed to determine reusability.

Run 1 in figure 4.5a represents the initial test of the immobilized substrate. It is clear that after inserting the urease immobilized substrate into the urea, an increase in the pH was observed. In order to determine the feasibility of reusing the immobilized substrate, the substrate was removed from the solution at the conclusion of the experiment and immersed in pH 7.3 sodium phosphate buffer for storage overnight at 4°C. The same experiment was run the following day determine if there had been a decrease in the catalytic activity of the immobilized enzyme after repeated use. The experiment was performed for a total of five cycles. The relative activity was determined by equation 4.1 and the values were reported (%) and shown in figure 4.5b:

$$Relative\ Activity = \frac{\Delta pH_{run,n}}{\Delta pH_{run,1}} \quad (4.1)$$

It is clear that after each cycle, the relative activity decreased indicating that either some urease was desorbed from the substrate or deactivated (mechanism unknown).

#### 4.2.3 Synthesis of $\text{TiO}_2$ using immobilized urease:

$\text{TiO}_2$  was synthesized using urease immobilized onto a gold substrate by inserting immobilized substrates into a reaction solution containing 0.001M TiBALDH and 0.5M urea. Multiple urease immobilized gold substrates were inserted into the reaction solution

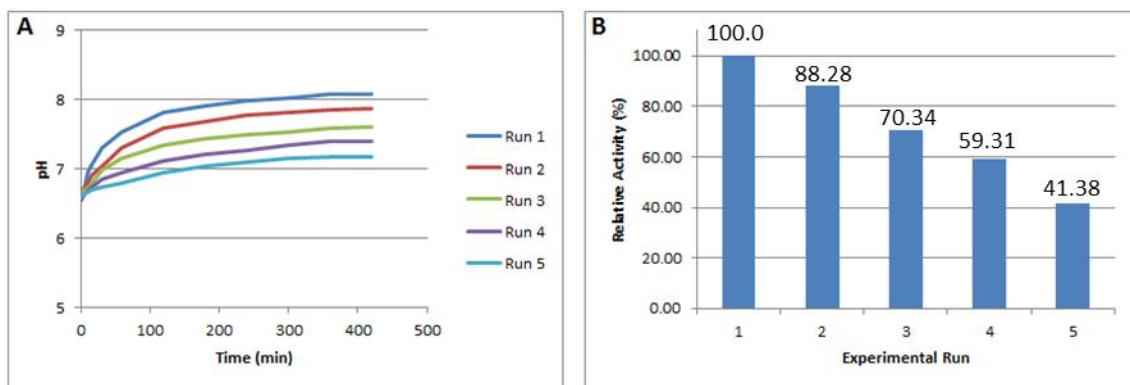


**Figure 4.5:** a) pH with respect to time plots for urease immobilized onto SAM functionalized gold substrate and b) relative activity per experimental cycle.

corresponding to approximate urease immobilized surface area of  $15\text{cm}^2$  (equated with a urease concentration of  $17.44\text{nM}$ ). The solutions were incubated at  $25^\circ\text{C}$  and magnetically stirred (700rpm) for 24hrs. The initial solution pH was 7.68 and the final pH = 8.81. TEM (Phillips, Tecnai12) was used to detect the presence of crystalline  $\text{TiO}_2$  in the as-synthesized material. After the 24hr reaction time, TEM specimens were prepared by depositing  $10\mu\text{L}$  of reaction solution directly onto a 400 mesh holey-carbon copper grids (Ted Pella).

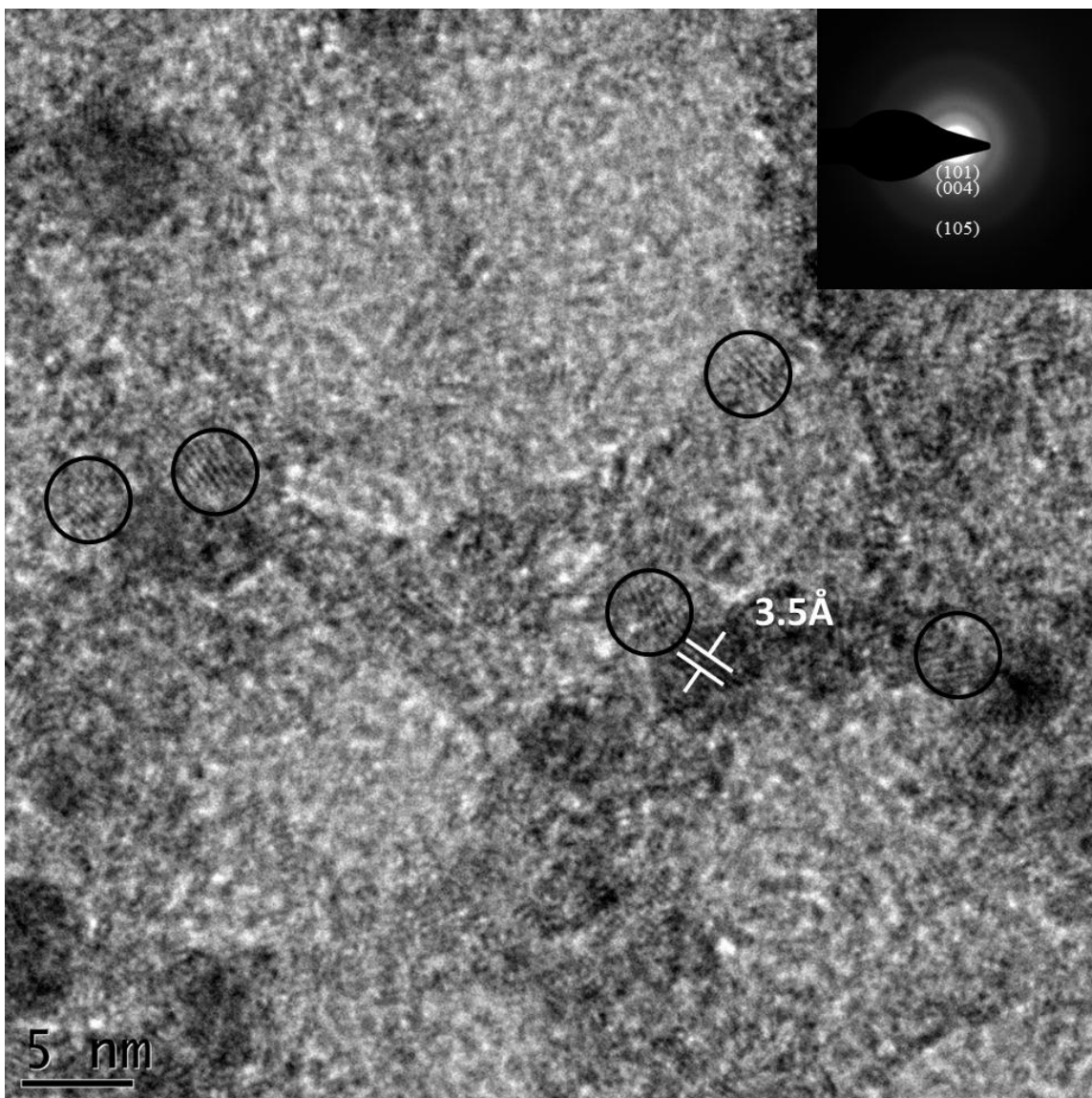


**Figure 4.6:** Bright field TEM image, with SAED inset of TiO<sub>2</sub> nanocrystals prepared at 25°C incubation for 24hrs using urease immobilized onto a gold substrate, the circles indicate apparent lattice fringes.

The solution reached a final pH of 8.81 at approximately 12 hours into the synthesis reaction. The solution became slightly opaque after approximately 20 hours of reaction time, indicating the presence of products in the reactor. Based on experiments using the free-floating enzyme for TiO<sub>2</sub> synthesis, it was determined that nucleation

occurs between pH 8.42 and pH 8.65, thus it is assumed that nucleation occurred within 12 hours after the immobilized enzyme had been introduced into the system. TEM images (fig. 4.6) showed nanocrystals of approximately 3nm, with measured d-spacings of  $3.51 \pm 0.03 \text{ \AA}$  corresponding to (101) anatase  $\text{TiO}_2$ . The presence of anatase  $\text{TiO}_2$  was further corroborated using SAED (fig. 4.6, inset).

The initial run from the reusability study showed a maximum pH achieved of 8.04. Based on the packing density of the urease conjugated gold substrates, determined from AFM analysis, the molarity of the solution with respect to urease for a single  $3\text{cm}^2$  wafer is 3.5nM. The immobilized urease synthesis solutions required the use of multiple wafers for a combined surface area of  $15\text{cm}^2$ , correlating to a 17.34nM urease concentration, in order to achieve pH levels conducive to  $\text{TiO}_2$  synthesis.

#### *4.3 Discussion/Conclusions*

Gold-coated silicon wafers were functionalized with an alkane thiol based self-assembled monolayer and conjugated to the urease enzyme via EDC/NHS coupling chemistry. The presence of enzyme, bound to the gold substrate surface, was verified by measurement of increasing pH, on introduction of urea to the reaction solution, and by observation of the urease conjugated surface using AFM. Reusability tests on the urease conjugated gold substrates showed that subsequent uses of the immobilized enzyme could produce measurable increases in solution pH, but that the achieved pH decreased with each successive use.

Initial change in pH with respect to time experiments showed that for a single 3cm<sup>2</sup> urease conjugated gold wafer, the highest pH achieved was 8.04. Previous TiO<sub>2</sub> synthesis experiments using free-floating urease showed that nucleation of anatase TiO<sub>2</sub> occurred in the pH range of approximately 8.42 to 8.65, thus in order to produce TiO<sub>2</sub> using immobilized urease, multiple urease conjugated wafers were used up to a urease immobilized surface area of 15cm<sup>2</sup>. This resulted in a maximum pH achieved of 8.81. Subsequent TEM analysis showed that materials synthesized were anatase TiO<sub>2</sub> of approximately 3nm in size.

## Chapter 5: Summary

The depletion of easily procured supplies of fossil fuels, presents a fundamental challenge for our planet. As these resources grow scarce in the coming decades, new renewable sources of energy would appear to be the logical replacement of the diminishing fossil fuel supply. However, most renewable forms of energy have displayed a pronounced low efficiency versus traditional fossil fuel based energy resources. In order to produce new energy efficiently and cost effectively, new synthesis methods need to be explored.

Another concern for the entire world is that of the diminishing supply of drinkable water. The growth of the pharmaceutical and personal care product industries, although extremely beneficial on the surface, has had the unintended consequences of contaminating our water supplies. New emerging contaminants are only now beginning to be understood and the long-term detrimental effects are yet to be determined. Thus, technologies need to be developed in the present in order to meet challenges that may arise in the future.

Semiconducting materials such as titanium dioxide have the distinction of being applicable to a multitude of applications. Specifically,  $\text{TiO}_2$  has shown great promise in both energy production, through photovoltaic application such as dye-sensitized solar cells, and photocatalytic destruction of organic contaminants present in waste waters.  $\text{TiO}_2$  is of further interest to researchers due to its low cost, abundance, and low environmental impact.

One of the main obstacles to wide-scale application of semiconducting materials, such as  $\text{TiO}_2$ , is the high cost associated with synthesizing these materials at the nanoscale with low size disparity. We have demonstrated a bio-mediated approach, using the hydrolytic enzyme urease, to induce a uniform dispersion of anatase  $\text{TiO}_2$  at room temperature. This is achieved through coordination of enzyme with urea in a solution containing a hydrolytically stable  $\text{TiO}_2$  precursor. The lag time between injection of urease and generation of hydroxide ions in solution affords a coordinated hydrolysis and condensation of precursor molecules, resulting in a single-burst nucleation event. In addition, the use of an enzyme to generate reagents (i.e., hydroxide ions) circumvents the need to thermally decompose formamide or urea, and thus, the reaction can be sustained at room temperature, which enables the growth of these materials on polymeric substrates (e.g., electrically conductive polymers as electrodes for flexible sensitized solar cells). The cost associated with the procurement of enzymatic reagents has resulted in low applicability for industrial processes. Thus, we have also demonstrated the feasibility of immobilizing the enzyme urease, for use in synthesis of nanoscale semiconducting materials such as titanium dioxide. Immobilization of the enzyme helps reduce the associated cost by providing a catalyst carrier which may be easily retrieved from synthesis solutions and reused for further catalytic reactions.

## References

- 1 Schlapbach, L.; Züttel, A. *Nature*. **2001**, *414*, 353-358.
- 2 Garzella, C.; Comini, E.; Tempesti, E.; Frigeri, C.; Sberveglieri, G. *Sens. Actuators B*. **2000**, *68*, 189-196.
- 3 Kinsinger, N.; Tantuccio, A.; Minwei, S.; Yan, Y.; Kisailus, D. *Journal of Nanoscience and Nanotechnology*. **2011**, *11*, 7015-7021.
- 4 Sauvage, F.; Di Fonzo, F.; Li Bassi, Li.; Casari, C. S.; Russo, V.; Divitni, G.; Ducati, C.; Bottani, C. E.; Comte, P.; Graetzel, M. *Nano. Lett.* **2010**, *10*(7), 2562-2567.
- 5 O'Neill, S. A.; Parkin, I. P.; Clark, R. J. H.; Mills, A.; Elliot, N. *J. Mater. Chem.* **2003**, *13*, 56-60
- 6 Giolli, C.; Borgioli, F.; Credi, A.; Di Fabio, A.; Fossati, A.; Miranda, M. M.; Parmeggiani, S.; Rizzi, G.; Scrivani, A.; Troglio, S.; Tolstoguzov, A.; Zoppi, A.; Bardi, U. *Surface and Coatings Technology*. **2007**, *202*, 13-22.
- 7 Gian, G. L.; Selli, E.; Forni, L. *Applied Catalysis B: Environmental*. **2008**, *84*, 332-339.
- 8 Andersson, M.; Osterlund, L.; Ljungstrom, S.; Palmqvist, A. *J. Phys. Chem. B*. **2002**, *106*, 10674-10679.
- 9 Wahi, R. K.; Liu, Y.; Falkner, J. C.; Colvin, V. L. *J. of Colloid Interface Sci.* **2006**, *302*, 530-536.
- 10 Antonelli, D. M.; Ying, J. Y.; *Angew. Chem. Int. Ed.* **2003**, *34*, 2014-2017.
- 11 World Coal Institute (WCI). *Coal Facts* 2009.
- 12 BP Energy Outlook 2030, January 2012.
- 13 Shafiee, S.; Topal, E. *Energy Policy*. **2008**, *36*, 775-786.
- 14 Larson, E. D. *Energy and Sustainable Development*. **2006**, *2*, 109-126.
- 15 Carrasco, J. M.; Franquelo, L. G.; Bialasiewicz, J. T.; Galvan, E.; Guisado, R. C. P.; Pratz, Ma. A. M.; Leon, J. I.; Moreno-Alfonso, N. *Industrial Electronics*. **2006**, *4*, 1002-1016.
- 16 Lund, J. W.; Freeston, D. H. *Geothermics*. **2001**, *30*, 29-68.
- 17 Gueymard, C. A. *Solar Energy*. **2004**, *76*, 423-453.
- 18 Schlettwein, D.; Yoshida, T.; Lincot, D. *Advances in Electrochemical Science and Engineering, Vol 12: Photoelectrochemical Materials and Energy Conversion Processes*. Weinheim: Wiley-VCH, **2010**, pp. 221.
- 19 International Energy Agency (2011) *Key World Energy Statistics*, International Energy Agency, Paris.
- 20 Linsebigler, A. L.; Lu, G.; Yates Jr., J. T. *Chem. Rev.* **1995**, *95*, 735-758.
- 21 Smestad, G. P. *Optoelectronics of Solar Cells*. Bellingham: SPIE, **2002**.
- 22 Yates Jr., J. T. *Surface Science*. **2009**, *603*, 1605-1612.
- 23 Crabtree, G. W.; Dresselhaus, M. S.; Buchanan, M. V. *Physics Today*. **2004**, *12*, 39-44.

- 24 Ashokkumar, M. *Int. J. Hydrogen Energy*. **1998**, *23*, 427-438.
- 25 Chen, X.; Mao, S. S. *Chemical Reviews*. **2007**, *107*, 2891-2959.
- 26 O'Regan, B.; Gratzel, M. *Letters to Nature*. **1991**, *353*, 737-740.
- 27 Carp, O.; Huisman, C. L.; Reller, A. *Progress in Solid State Chemistry*. **2004**, *32*, 33-177.
- 28 Abe, R.; Sayama, K.; Arakawa, H. *Chemical Physics Letters*. **2002**, *362*, 441-444.
- 29 Ni, M.; Leung, M. K. H.; Leung, D. Y. C.; Sumathy, K. *Renewable and Sustainable Energy Reviews*. **2007**, *11*, 401-425.
- 30 Hemmett, R. USEPA Region 2 presentation, "Emerging Contaminants Identification Concerns Actions"
- 31 Kummerer, K. *Chemosphere*. **2001**, *45*, 957-969.
- 32 Ivashechkin, P.; Corvini, P. F.; Dohmann, M. *Water Sci Technol*. **2004**, *50(5)*, 133-140
- 33 Diamanti-Kandarakis, E.; Bourguignon, J.; Giudice, L. C.; Hauser, R.; Prins, G. S.; Soto, A. M.; Zoeller, R. T.; Gore, A. C. *Endocrine Reviews*. **2009**, *30*, 293-342.
- 34 Daughton, C. G. *Environ Impact Assess Rev*. **2004**, *24*, 711-732.
- 35 Kolpin, D. W.; Furlong, E. T.; Meyer, M. T.; Thurman, E. M.; Zaugg, S. D.; Barber, L. B.; Buxton, H. *Environ Sci Technol*. **2002**, *36*, 1202-1211.
- 36 Gogate, P. R.; Pandit, A. B. *Advances in Environmental research*. **2004**, *8*, 501-551.
- 37 Bahnemann, D. *Solar Energy*. **2004**, *77*, 445-459.
- 38 Al-Ekabi, H.; Serpone, N. *Langmuir*. **1989**, *5*, 250-255.
- 39 Ahmed, S.; Rasul, M. G.; Brown, R.; Hashib, M. A. *Journal of Environmental Management*. **2011**, *92*, 311-330.
- 40 Lim, S. H.; Luo, J.; Zhong, Z.; Ji, W.; Lin, J. *Inorg. Chem*. **2005**, *44*, 4124-4126.
- 41 Jun, Y.; Kim, H.; Lee, J.; Hong, S. *Sensors and Actuators B*. **2005**, *107*, 264-270.
- 42 Ruiz, A. M.; Sakai, G.; Cornet, A.; Shimanoe, K.; Morante, J. R.; Yamazoe, N. *Sensors and Actuators B: Chemical*. **2003**, *93*, 509-518.
- 43 Jun, Y.; Kim, H.; Lee, J.; Hong, S. *Sensors and Actuators B*. **2006**, *120*, 69-73.
- 44 Nechita, V.; Schoonman, J.; Musat, V. *Phys. Status Solid A*. **2012**, *209*, 153-159.
- 45 Penn, R. L.; Banfield, J. F. *American Mineralogist*. **1999**, *84*, 871-876.

- 46 Burdett, J. K.; Hughbanks, T.; Miller, G. J.; Richardson, J. W.; Smith, J. V. *J. Am. Chem. Soc.* **1987**, *109*, 3639-3646.
- 47 Hurum, D. C.; Agrios, A. G.; Gray, K. A.; Rajh, T.; Thurnaur, C. *Journal of Physical Chemistry B.* **2003**, *107*, 4545-4549.
- 48 Matsumoto, H.; Uchida, H.; Yoneyama, H. *Res. Chem. Intermed.* **1994**, *20*, 723-733.
- 49 Jiang, J. G.; Liu, H.; Guo, L. J. *The 6<sup>th</sup> International Symposium on Multiphase Flow, Heat Mass Transfer and Energy Conversion.* **2010**, 1053-1059.
- 50 Harris, C.; Kamat, P. *ACS Nano.* **2009**, *3*, 682-690.
- 51 Mills, A.; Le Hume, S. *Journal of Photochemistry and Photobiology A: Chemistry.* **1997**, *108*, 1-35.
- 52 Tsuji, I.; Kudo, A. *Journal of Photochemistry and Photobiology A: Chemistry.* **2003**, *156*, 249-252.
- 53 Hu, J.; Ren, L.; Guo, Y.; Liang, H.; Cao, A.; Wan, L.; Bai, C. *Angew. Chem. Int. Ed.* **2005**, *44*, 1269-1273.
- 54 Bahnemann, D. W.; Kormann, C.; Hoffmann, M. R. *J. Phys. Chem.* **1987**, *91*, 3789-3798.
- 55 Hoffmann, M. R.; Martin, S. T.; Choi, W.; Bahnemann, D. W. *Chem. Rev.* **1995**, *95*, 89-96.
- 56 Park, J.; Sudarshan, T. S. *Chemical Vapor Deposition.* Materials Park: ASM International, **2001**.
- 57 Nakaso, K.; Okuyama, K.; Shimada, M.; Pratsinis, S. E. *Chemical Engineering Science.* **2003**, *58*, 3327-3335.
- 58 Kim, C. S.; Nakaso, K.; Xia, B.; Okuyama, K.; Shimada, M. *Aerosol Science and Technology.* **2005**, *39*, 104-112.
- 59 Xiang, B.; Zhang, Y.; Wang, Z.; Luo, X. H.; Zhu, Y. W.; Zhang, H. Z.; Yu, D. P. *Journal of Physics D: Applied Physics.* **2005**, *38*, 1152-1155.
- 60 Khan, S. U. M.; Al-Shahry, M.; Ingler Jr., W. B. *Science.* **2002**, *297*, 2243.
- 61 Bickmore, C. R.; Waldner, K. F.; Baranwal, R.; Hinklin, T.; Treadwell, D. R.; Laine, R. M. *Journal of the European Ceramic Society.* **1998**, *18*, 287-297.
- 62 Augugliaro, V.; Loddo, V.; Pagliaro, M.; Palmisano, G.; Palmisano, L. *Clean by Light Irradiation: Practical Applications of Supported TiO<sub>2</sub>.* Cambridge, RSC Publishing, **2010**.
- 63 Zhang, Z.; Wand, C.; Zakaria, R.; Ying, J. Y. *Journal of Physical Chemistry B.* **1998**, *102*, 10871-10878.

- 64 Cushing, B. L.; Kolesnichenko, V. L.; O'Connor, C. J. *Chemical Reviews*. **2004**, *104*, 3893-3946.
- 65 Livage, J.; Henry, M.; Sanches, C. *Prog. Solid. St. Chem.* **1988**, *18*, 259-341.
- 66 Brinker, C. J.; Scherer, G. W. *Sol-gel science*. Boston: Academic Press, **1990**, pp. 23.
- 67 Livage, J.; Sanchez, C.; Henry, M.; Doeuff, S. *The Chemistry of the Sol-Gel process*, **1989**, *32/33*, 633-638.
- 68 Niederberger, M.; Pinna, N. *Metal Oxide nanoparticles in Organic Solvents: Synthesis, Formation, Assembly and Application*. London: Springer-Verlag, **2009**.
- 69 Park, J.; An, K.; Hwang, Y.; Park, J. G.; Noh, H.; Kim, J.; Park, J. H.; Hwang, N.; Hyeon, T. *Nature Materials*. **2004**, *3*, 891-895.
- 70 Wang, C.; Ying, J. Y. *Chemistry of Materials*, **1999**, *11*, 3113-3120.
- 71 Cao, G.; Wang, Y. *Nanostructures and Nanomaterials: Synthesis, Properties, and applications*. London: Imperial College Press, **2011**.
- 72 Chen, X.; Wang, J.; Hu, H.; Fu, F.; Shu, H.; Yang, M.; Du, G. X.; Yao, Y. *Journal of Inorganic Chemistry*. **2007**, *633*, 2053-2058.
- 73 Cheng, H.; Ma, J.; Zhao, Z.; Qi, L. *Chemistry of Materials*. **1995**, *7*, 663-671.
- 74 Li, X.; Peng, Q.; Yi, J.; Wang, X.; Li, Y. *Chem. Eur. J.* **2006**, *12*, 2383-2391.
- 75 Finnegan, M. P.; Zhang, H.; Banfield, J. F. *J. Phys. Chem. C.* **2007**, *111*, 1962-1968.
- 76 Schwenzer, B.; Neilson, J. R.; Jeffries, S. M.; Morse, D. E. *Dalton Trans.* **2011**, *40*, 1295-1301.
- 77 Fogler, H. S. *Elements of Chemical Reaction Engineering*. 4<sup>th</sup> ed, Upper Saddle River: Pearson Education Inc. **2008**, pp. 398.
- 78 Willard, H. H.; Tang, N. K. *Journal of the American Chemical Society*. **1937**, *7*, 1190-1196.
- 79 Rajamathi, M.; Kamath, P. V. *International Journal of Inorganic Materials*. **2001**, *7*, 901-906.
- 80 Yang, R.; Yu, H.; Li, M. *Journal of Materials Science Letters*. **2003**, *22*, 1131-1135.
- 81 Shimizu, K.; Cha, J.; Stucky G. D.; Morse, D. E. *Proc. Natl. Acad. Sci. U. S. A.* **1998**, *95*, 6234-6238.
- 82 Matijevic, E. *Chem Mater*. **1993**, *5*, 412-426.
- 83 Umetsu, M.; Mizuta, M.; Tsumoto, K.; Ohara, S.; Takami, S.; Watanabe, H.; Kumagai, I.; Adschiri, T. *Adv. Mater.* **2005**, *17*, 2571-2575.
- 84 Thai, C. K.; Dai, H.; Sastry, M. S. R.; Sarikaya, M.; Schwartz, D. T.; Baneyx, F. *Biotechnol. Bioeng.* **2004**, *87*, 130-137.

- 85 Kisailus, D.; Choi, J. H.; Weaver, J. C.; Yang, W.; Morse, D. E. *Adv. Mater.* **2005**, *17*, 314-318.
- 86 Sumerel, J. L.; Yang, W.; Kisailus, D.; Weaver, J. C.; Choi, J. H.; Morse, D. E. *Chem. Mater.* **2003**, *15*, 4804-4809.
- 87 Kroger, N.; Dickerson, M. B.; Ahmad, G.; Cai, Y.; Haluska, M. S.; Sandhage, K. H.; Poulsen, N.; Sheppard, V.C. *Angew. Chem., Int.* **2006**, *45*, 7239-7243.
- 88 Luckarift, H. R.; Dickerson, M. B.; Sandhage, K. H.; Spain, J. C. *Small.* **2006**, *5*, 640-643.
- 89 Gopal, M.; Moberly Chan, W. J.; De Jonghie, L. C.; *J. Mater. Sci.* **1997**, *22*, 6001-6008.
- 90 Adachi-Pagano, M.; Forano, C.; Besse, J. *J. Mater. Chem.* **2003**, *13*, 1988-1993.
- 91 Kisailus, D.; Schwenzer, B.; Gomm, J.; Weaver, J.C.; Morse, D. E. *J. Am. Chem. Soc.* **2006**, *128*, 10276-10280.
- 92 Schwenzer, B.; Roth, K. M.; Gomm, J. R.; Murr, M.; Morse, D. E. *J. Mater. Chem.* **2006**, *16*, 401-407.
- 93 Kometani, N.; Fujita, A.; Yonezawa, Y. *J. Mater. Sci.* **2008**, *43*, 2942-2498.
- 94 Yang, R.; Yu, H.; Li, M. *J. Mater. Sci. Lett.* **2003**, *22*, 1131-1135.
- 95 Rajamathiand, M.; Kamath, P. V. *Int. J. Inorg. Mater.* **2001**, *3*, 901-906.
- 96 Jeong, Y.-K.; Shin, D.-K.; Lee, H.-J.; Oh, K.-S.; Lee, J.-H.; Riu, D.-H. *Key Engineering Materials.* **2006**, *317*, 203-206.
- 97 Cesareo, S. D.; Langton, S. R. *FEMS Microbiol. Lett.* **1992**, *99*, 15-22.
- 98 Lippard, S. J. *Science*, **1995**, *268*, 996-997.
- 99 Mobley, H. L. T.; Island, M. D.; Hausinger, R. P. *Microbiol. Rev.* **1995**, *59*, 451-480.
- 100 Sumner, J. B.; *J. Biol. Chem.* **1926**, *69*, 435-441.
- 101 Dixon, N. E.; Gazzola, C.; Blakeley, R. L.; Zerner, B. *J. Am. Chem. Soc.* **1975**, *97*, 4131.
- 102 Balasubramanian, A.; Ponnuraj, K. *J. Mol. Biol.* **2010**, *400*, 274-283.
- 103 Carter, E. C.; Flugga, N.; Boer, J. L.; Mulrooney, S. B. *Meallomics.* **2009**, *1*, 207-221.
- 104 Carlsson, H.; Nordlander, E. *Bioinorganic Chemistry and Applications.* **2010**, *2010*, 1-8.
- 105 Mockel, H.; Giersig, M.; Willig, F. *J. Mater. Chem.* **1999**, *9*, 3051-3056.
- 106 Casey, W. H.; Phillips, B. L.; Nordin, J. P.; Sullivan, D. J. *Geochemica.* **1998**, *62*, 2789-2797.
- 107 Kinsinger, N. M.; Wong, A; Li, D.; Villalobos, F.; Kisailus, D. *Crystal Growth and Design.* **2010**, *10*, 5254-5261.
- 108 Krajewska, B.; Chudy ,M.; Drozdek, M.; Brzozka, Z. *Electroanalysis*, **2003**, *15*, 5-6.
- 109 Lai, C. M.; Tabatabai, M. A. *Soil. Boil. Biochem.* **1992**, *24*, 225-228.
- 110 Cevik, E.; Senel, M.; Abasiyank, M. F. *Afr. J. Biotechnol.* **2011**, *10*, 6590-6597.

- 111 Murakami, N.; Kurlhara, Y.; Tsubota, T.; Ohno, T. *J. Phys. Chem. C*. **2009**, *113*, 3062-3069.
- 112 Madhusudan Reddy, K.; Manorama, S.V.; Ramachandra Reddy, A. *Mater. Chem. Phys.* **2003**, *78*, 239-245.
- 113 Almquist, C. B.; Biswas, P. *Journal of Catalysis*. **2002**, *212*, 145-146.
- 114 Li, M.; Li, J. C. *Materials Letters*. **2006**, *60*, 2526-2529.
- 115 Voorhees, P. W. *Journal of Statistics*. **1985**, *38*, 231-252.
- 116 Penn, R. L.; Banfield, J. F. *Geochimica et Cosmochimica Acta*. **1999**, *63*, 1549-1557.
- 117 Finnigan, M. P.; Zhang, H.; Banfield, J. F. *Chemistry of Materials*. **2008**, *20*, 3443-3449.
- 118 Matthews, A. *Amer. Miner.* **1976**, *61*, 419-424.
- 119 Okada, K.; Yamamoto, N.; Kameshima, T.; Yasumori, A. *J. Am. Chem. Soc.* **2001**, *84*, 1591-1596.
- 120 Shin, H.; Jung, H. S.; Hong, K. S.; Lee, J.-K. *J. Solid State Chem.* **2005**, *178*, 15-21.
- 121 Matthews, A. *Amer. Miner.* **1976**, *61*, 419-424.
- 122 Ghosh, T. B.; Dhabal, S.; Datta, A. K. *J. Appl. Phys.* **2003**, *94*, 4577-4582.
- 123 Zhang, H. Z.; Banfield, J. F.; *J. Mat. Chem.* **1998**, *8*, 2073-2076.
- 124 Garcia-Ruiz, J. M. *Journal of Structural Biology*. **2003**, *142*, 22-31.
- 125 De Yoreo, J. J.; Vekilov, P. G. *Rev. Mineral. Geochem.* **2003**, *54*, 57-93.
- 126 Bastow, T. J.; Moodie, A. F.; Smith, M. E.; Whitfield, H. J. *J. Mater. Chem.* **1993**, *3*, 697.
- 127 Madhusudan Reddy, K.; Manorama, S.V.; Ramachandra Reddy, A. *Mater. Chem. Phys.* **2003**, *78*, 239-245.
- 128 Tischer, W.; Wedekind, F. *Topics in Current Chemistry*. **1999**, *200*, 96-123.
- 129 Anita, A.; Sastry, C. A.; Hashim, M. A. *Bioprocess and Biosystems Engineering*. **1997**, *17*, 355-359.
- 130 Ottolina, G.; Carrea, G.; Riva, S.; Sartore, L.; Veronese, F. M. *Biotechnology Letters*. **1992**, *10*, 947-952.
- 131 Schmidtke, J. L.; Westcott, C. R.; Klibanov, A. M. *J. Am. Chem. Soc.* **1996**, *118*, 3360.
- 132 Taylor, R. H.; Fournier, S. M.; Simons, B. L.; Kaplan, H.; Hefford, M. A. *Journal of Biotechnology*. **2005**, *118*, 265-269.
- 133 Costa, S. A.; Tsanov, T.; Paar, A.; Gudelj, M. Gubitza, G. M.; Cavaco-Paulo, A. *Enzyme and Microbial Technology*. **2001**, *28*, 815-819.
- 134 Bao, H.; Lui, T.; Zhang, L.; Chen, G. *Proteomics*. **2009**, *9*, 1114-1117.
- 135 Coulet, P. R.; Gautheron, D. C. *Journal of Chromatography A*. **1981**, *215*, 65-72.
- 136 D'Urso, E. M.; Fortier, G. *Biotechnology Techniques*. **1994**, *8*, 71-76.

- 137 Hsiao, H.; Royer, G. P. *Archives of Biochemistry and Biophysics*. **1979**, *198*, 379-385.
- 138 Goel, M. K. *Immobilized Enzymes*. **1994**, New York/Rensselaer Polytechnic Institute. Unpublished.
- 139 Sheldon, R. A. *Adv. Synth. Catal.* **2007**, *349*, 1289-1307.
- 140 Avnir, D.; Braun, S.; Lev, Ovadia,; Ottolenghi, M. *Chem. Mater.* **1994**, *6*, 1605-1614.
- 141 Naik, R. R.; Tomczak, M. M.; Luckarift, H. R.; Spain, J. C.; Stone, M. *Chem. Commun.* **2004**, 1684-1685.
- 142 Trevan, M. D. *New Protein Techniques: Enzyme Immobilization by Entrapment*. **1988**, *3*, 491-494.
- 143 Bain, C. D.; Biebuyck, H. A.; Whitesides, G. M. *Langmuir*. **1989**, *5(3)*, 723-727.
- 144 Bain, C. D.; Troughton, E. B.; Tao, Y.-T.; Evall, J.; Whitesides, G. M.; Nuzzo, R. G. *J. Am. Chem. Soc.* **1989**, *111*, 321-335.
- 145 Bain, C. D.; Whitesides, G. M. *J. Am. Chem. Soc.* **1988**, *110*, 6560.
- 146 Aizenber, J.; Black, A. J.; Whitesides, G. M. *Nature*. **1988**, *394*, 868-871.
- 147 Dubois, L. H.; Nuzzo, R. H. *Annual Review of Physical Chemistry*. **1992**, *43*, 437-463.
- 148 Sam, S.; Touahir, L.; Andresa, J. S.; Allongue, P.; Chazalviel, J.-N.; Gouget-Laemmel, A. C.; de Villeneuve, H.; Moraillon, A.; Ozanam, F.; Gabouze, N.; Djebbar, S. *Langmuir*. **2010**, *26(2)*, 809-814.
- 149 Nakajima, N.; Ikada, Y. *Bioconjugate Chem.* **1995**, *6(1)*, 123-130.
- 150 Sehgal, D.; Vijay, I. K. *Anal. Biochem.* **1994**, *218(1)*, 87-91.
- 151 Rusmini, F.; Zhong, Z.; Feijen, J. *Biomacromolecules*. **2007**, *8(6)*, 1775-1789.
- 152 Tiwari, A. *Journal of Inorganic and Organometallic Polymers and Materials*. **2009**, *19*, 361-366.
- 153 Yun, D.-H.; Song, M.-J.; Hong, S.-I. *Journal of the Korean Physical Society*. **2005**, *47*, 445-449.
- 154 Alqasaimh, M. S.; Heng, L. Y.; Ahmed, M. *Sensors*. **2007**, *7*, 2251-2262.
- 155 Di Martino, S.; El-Sheriff, H.; Diano, N.; De Maio, A.; Grano, V.; Rossi, S.; Bencivenga, U.; Mattei, A.; Mita, D. G. *Applied Catalysis B: Environmental*. **2003**, *46*, 613-629.
- 156 Blakely, R. L.; Zerner, B. *Journal of Molecular Catalysis*. **1984**, *23*, 263-292.